Stockholm University

Master Thesis

Degree Project in Marine Geology 45 hp

Southern Ocean paleoceanographic changes at the Eocene-Oligocene climate transition: a meridional deep-sea transect of the Kerguelen Plateau

Natalia Barrientos

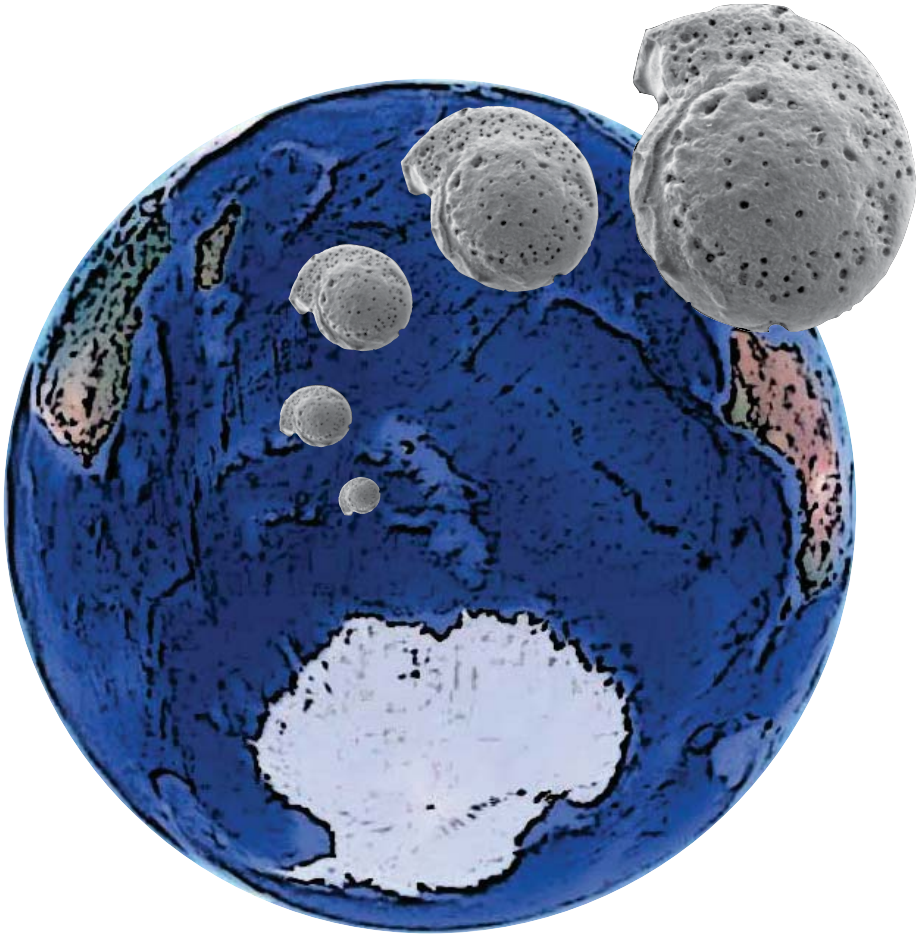

Stockholm 2013

Department of Geological Sciences
Stockholm University
SE-106 91 Stockholm

Abstract.
This thesis investigates paleoceanographic changes from the late Eocene - early Oligocene climate transition (EOT) on the Kerguelen Plateau (KP) submerged igneous province in the Southern Indian Ocean. This transition is characterized by the onset of permanent ice-sheets over Antarctica. However, forces and feedbacks of this glaciation on Southern Ocean circulation remains focus of debate.

At present, the Antarctic Polar Front is located at the northern part of the KP where the cold northward-flowing Antarctic waters converge and sink below warmer waters of the sub-Antarctic. This results in a narrow circumpolar oceanic belt extremely high in primary productivity, that shows a shift from biocalcareous sedimentary deposits to the north and biosiliceous to the south. In this thesis, the position of the Polar Front across the KP is studied. This is to test the hypothesis that the Polar Front shifted northward across the KP at the EOT, because of a change in the latitudinal thermal gradient between equator and pole driven by the impact of Antarctica glaciation. To achieve that, I have produced new paleoceanographic data for three ODP sites drilled during Leg 183 (Sites 1138, 1139 and 1140). The sites cover the northern and central latitudinal transect of the KP. The lithological characteristics at these sites are analyzed and the first high-medium resolution benthic foraminifera stable isotope records are generated from central and northern KP. The obtained isotope records are correlated with available records from southern KP (Sites 748, 744 and 738) from the late Eocene and early Oligocene to produce a paleoceanographic N-S transect spanning $\sim 20^{\circ}$ of latitude. The results of this synthesis show that regional northern KP intermediate waters at the three new sites have similar oxygen isotope values compared to southern KP sites in the latest Eocene. This suggests the location of the Polar Front south of the KP with warm Indian Ocean conditions extended over KP. Conversely, there are differences in the oxygen isotope values between the three new sites and southern KP at the earliest Oligocene. This is coeval with a biosilica facies change found at southern KP during EOT. Finally, the results are incorporated into a larger framework where the KP isotope records are compared with records from the Atlantic sector of the Southern Ocean and globally. Latitudinal variations along the Southern Ocean were observed suggesting relative colder intermediate/bottom waters at sites close to the Antarctic continent until reaching central KP, indicating that the Antarctic Polar Front, if present as we know it today, was located between central and southern KP at the EOT.

Contents

Chapter 1

Introduction

One of the most significant paleoclimatic changes of the Cenozoic occurred close to the Eocene/Oligocene climate transition (EOT), $\sim$ 34 Ma. Earth underwent a fundamental transition from 'greenhouse' to 'icehouse' climate conditions that characterizes our modern climate system. This abrupt shift is associated with the onset of permanent ice-sheets over East Antarctica (e.g. Kennett and Shackleton, 1976; Miller et al., 1991; Coxall et al., 2005; Lear et al., 2008). Among the possible triggering mechanisms for this glaciation are: (i) orbital insolation changes promoting snow accumulation in the absence of warm summers (Coxall et al., 2005); (iii) decrease in atmospheric CO_2 that post a threshold for continental glaciation (DeConto and Pollard, 2003; DeConto et al., 2008; Pagani et al., 2011); (iii) paleogeographic reconfigurations through the widening of Drake Passage and Tasmanian Gateway favoring the change of a meridional to circum-Antarctic current circulation (ACC) (Kennett and Shackleton, 1976; Kennett, 1977; Stickley et al., 2004; Scher and Martin, 2006; Eagles et al., 2006), which is still fiercely debated (Sijp et al., 2009; 2011; Zhang et al., 2011; Yang et al., 2013). To optimize paleoclimate models and hence future climatic predictions, it is important to target both the forcing mechanisms and feedbacks associated with initial Antarctic glaciation.

Since the 1970s, southern hemisphere glaciation and a global cooling event have been revealed by numerous studies of deep-sea sediment cores. The key evidence obtained from these marine records includes: (i) $>$ 1.0‰ increase in oxygen and carbon stable isotopes in benthic foraminifera calcite; (ii) deepening in the calcite compensation depth; in cores proximal to Antarctica (iii) co-occurrence of ice rafted debris; (iv) clay mineral shift from enhanced Antarctica weathering.

The Kerguelen Plateau (KP) is located in the Indian sector of the Southern Ocean (SO). It is classified as the second largest oceanic igneous plateau. KP formed though hotspot volcanism with large basaltic emplacements in different pulses: $\sim$110 Ma for southern KP (SKP), $\sim$ 85 Ma for central KP (CKP) and $\sim$ 40 Ma for northern KP (Coffin et al., 2000). It extends over almost 20°S latitudes (from 46°S to 64°S). The average modern water depths at the KP range from 1500 m in the north to 2500 m in the south which allowed the preservation of biogenic carbonate well above the Cenozoic lysocline. This shallow bathymetry is thought to constitute a major barrier to the current ACC (Park et al., 2008). Therefore, KP sits in a target area to investigate past changes in SO circulation at the EOT. This study will investigate the EOT sequences of three deep-sea sediment cores drilled during ODP Leg 183 in NKP (Site 1140, 1139) and CKP (Site 1138).

Existing foraminiferal oxygen and carbon stable isotope records from SKP indicate a decline in surface water temperatures predating the early Oligocene East Antarctica glaciation (Barrera and Huber, 1991). This coincides with sedimentary evidence for enhanced primary productivity showing a switch from biogenic calcite to biogenic silica during the earliest Oligocene (Diester-Haass, 1996; Salamy and Zachos, 1999). Associated with this is an increase in benthic foraminifera accumulation rates and deterioration of carbonate preservation (Diester-Haass, 1996; Diester-Haass and Zahn, 1996). These changes are suggested to reflect the northward migration of a polar front over the southern end of the Kerguelen Plateau (Barrera and Huber, 1991; Salamy and Zachos, 1999) attributed to the establishment of new cold and nutrient-rich water masses associated with climate cooling. The cause of this is thought to be enhanced ocean and atmospheric circulation because of an increase in the latitudinal temperature gradient reflecting the migration of a polar front. This suggests a source of force or feedback on Antarctica glaciation, since the role of SO frontal upwelling zones and associated increase in productivity might have increase carbon cycling bringing a CO_2 drawdown.

1.1 Hypothesis and aims

This research investigates the following hypothesis:

"The Polar Front shifted northward across the Kerguelen Plateau at the EOT, because of a change in the latitudinal thermal gradient between equator and pole driven by the impact of Antarctica glaciation", Figure 1.1.

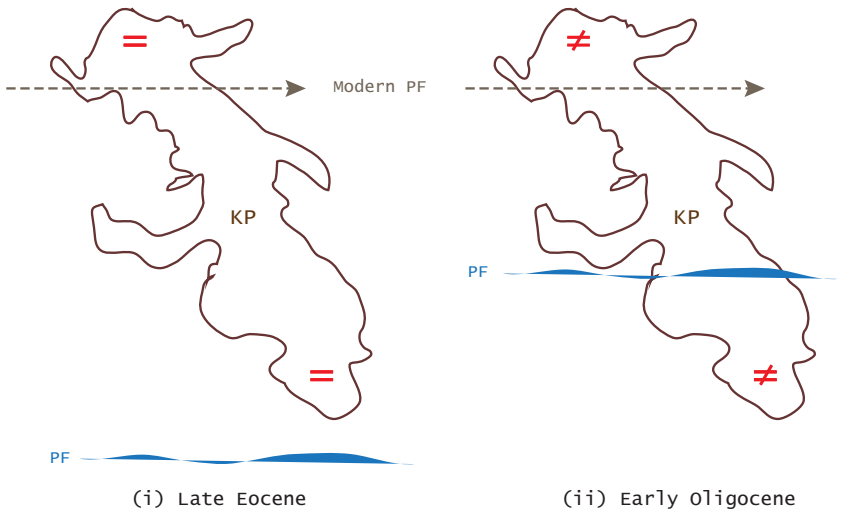

Figure 1.1: Two predicted scenarios of the hypothesis to be tested regarding paleo-ocean circulation and the relative location of the Antarctic PF: (i) late Eocene, similar north-south paleoceanographic conditions because the PF was located south of the KP; (ii) early Oligocene, different north-south paleoceanographic conditions because the PF had shifted northward dividing conditions across the KP. Modern Polar Front path after Orsi et al. (1995). PF: Polar Front, KP: Kerguelen Plateau.

In order to test the hypothesis this study aims to:

• Broad aims:

- Reconstruct latitudinal changes in SO deep circulation by comparing the three new benthic foraminifera stable isotope records to published records from SKP, Sites 748 (Zachos et al., 1992; 1994), 744 (Zachos et al., 1996) and 738 (Barrera and Huber, 1991). This suite of six sites provides the first deep-sea paleoclimate latitudinal chemostratigraphic transect across the KP.

- Contrast KP deep ocean elsewhere in the Southern Ocean (Atlantic sector) and globally.

• Specific aims:

- Produce an EOT latitudinal transect across the KP by adding three new sites from the northern part of KP containing the E/O boundary.

- For each site, add climate proxy data from stable isotopes producing the first carbon and oxygen isotope records in benthic foraminifera shells. The idea was that the oxygen isotope (δ^{18}O) records across the north-south KP transect will reveal if there were major differences in ocean-climate conditions from North to South and from the late Eocene to early Oligocene when Antarctica became glaciated. The record from carbon isotopes (δ^{13}C) will provide information on local paleoproductivity, global carbon burial and past deep-water mass movement.

- Revise the bio- and magnetostratigraphic chronologies for the three new sites based on the new isotopic records themselves since they reflect globally synchronous processes during the EOT.

- Constrain surface water conditions from lithological/biomineral facies changes and productivity proxies at the three new sites and compared them with the rest of the available sites.

Chapter 2

Background

2.1 The Eocene/Oligocene climate transition: geochronology and oxygen isotope signature

The Eocene-Oligocene climate transition (EOT) spans the boundary between the Eocene and Oligocene epochs. The EOT has long been known to be a time of major biotic and environmental change on land and in the oceans (Coxall and Pearson, 2007). The age of the Eocene/Oligocene (E/O) boundary is represented at 33.7 Ma by a golden spike for the global boundary stratotype sections and point (GSSP) on the geomagnetic polarity reversal timescale of Berggren et al. (1995) or 33.9 Ma on the timescale of Cohen et al. (2013). The E/O GSSP is located in Massignano quarry in Ancona (Italy), and it is based upon the extinction of the planktonic foraminiferal genus *Hantkenina*, a low to mid latitude taxon with restricted occurrence (Premoli-Silva and Jenkins, 1993). Some authors argue that the GSSP should be reselected since its age is older than the global oceanic oxygen isotope excursion, not represented in the current section (Van Mourik and Brinkhuis, 2005). However, it has been shown that this extinction actually occurs during the intermediate plateau of the two-step δ^{18}O that defines the EOT (Coxall and Pearson, 2007).

The most distinctive feature of the EOT in deep-sea records is a $> 1‰$ increase in the oxygen stable isotopic composition of benthic foraminifera calcite (δ^{18}O) (Zachos et al., 1994). This δ^{18}O increase happened globally and was synchronous. It lasted $\sim$ 500 ka with maximum values occurring in the basal Oligocene for $\sim$ 400 ka, roughly the duration of magnetic Chron C13n (e.g. Miller et al., 1987; Zachos et al., 1994; 1996) (see Figure 2.1 for the nomenclature and systematics of the climatic shift). This highest positive excursion in δ^{18}O is termed Oi-1 (Miller et al., 1991) and it comprises two maximum peaks namely Oi-1a and Oi-1b associated with two main glaciation pulses on Antarctica (Zachos et al., 1996; Salamy and Zachos, 1999). A detailed high resolution orbitally-tuned record revealed that the total isotopic shift occurred in two steps of less than 40 ka each that are separated by a 200 ka intermediate plateau (Coxall et al., 2005) where the extinction of *Hantkenina* occurred (Coxall and Pearson, 2007) (Figure 2.1). *Hantkenina* did not exist as far south as the latitudes of the true KP region, therefore it cannot be used to identify the E/O boundary in this study. Instead, the E/O boundary at the KP was approximated based on alternative calcareous nannofossil and planktonic foraminifera bioevents (Coffin et al., 2000; Huber, 1991).

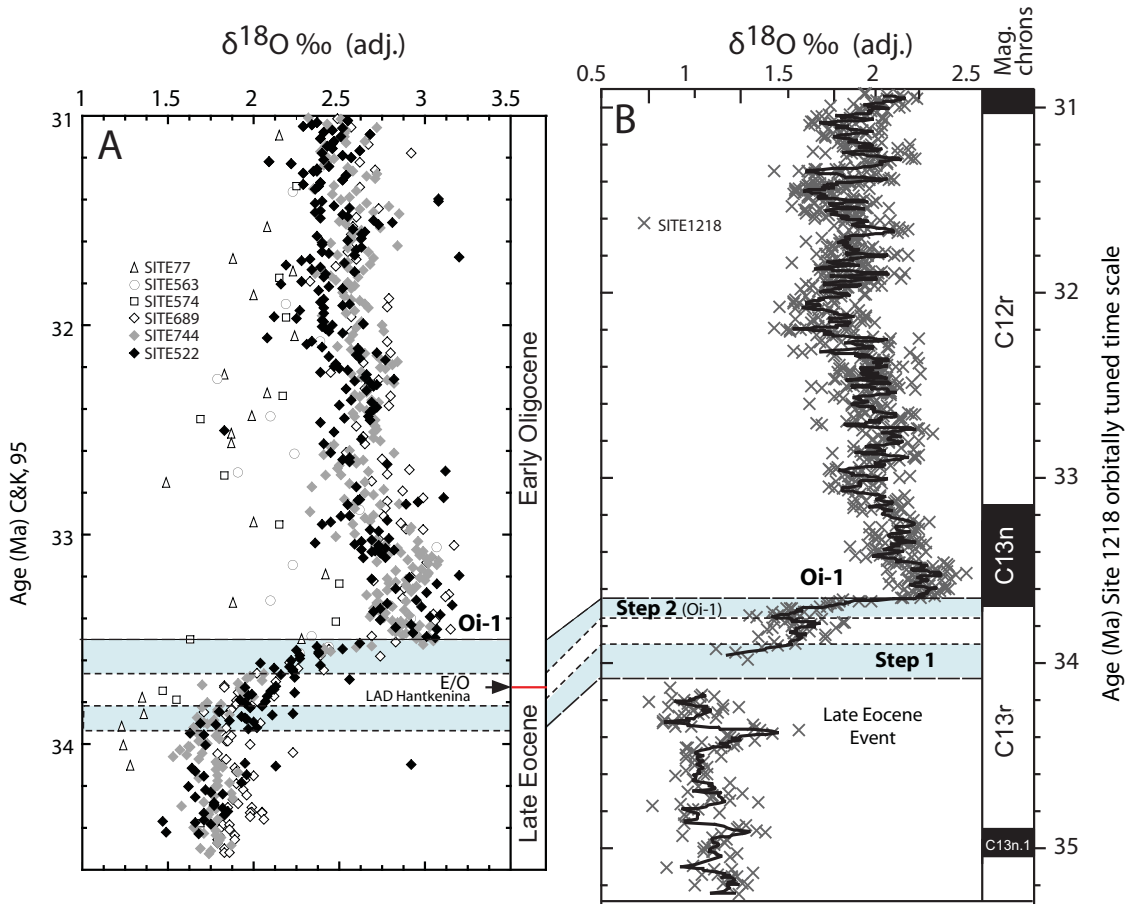

Figure 2.1: Nomenclature of the oxygen isotope events at the Eocene-Oligocene transition (EOT). After Coxall and Pearson (2007); Coxall and Wilson (2011). These records provide a reference template for interpreting the KP records produced in this study.

2.2 Geological Setting

The Kerguelen Plateau (KP) is a broad (200 to 600 km W-E) and long ($\sim$ 2300 km N-S) bathymetric elevation on the Southern Ocean (SO) that extends over a great latitudinal extent, from 46°S to 64°S ($\sim$ 18° of latitude). It is located on the Antarctic Plate and stands 24 km above the adjacent southern Indian Ocean and Southern Ocean basins (Coffin et al., 2000). The KP is divided into four distinct domains: the Elan Bank (EB), southern KP (SKP), central KP (CKP), and northern KP (NKP) that were formed in the Cretaceous and Paleogene. The Broken Ridge (BR), today located at 30°S and $\sim$ 2500 km to the north-east of KP, and CKP are conjugate Late Cretaceous provinces that were separated by seafloor spreading at $\sim$ 40 Ma, see Figure 2.2 (Coffin et al., 2000).

The KP together with the BR and Ninetyeast Ridge (NR) are classified as a large igneous province formed from a local vast injection of mantle-derived magma into the Earth's crust (Morgan, 1981; Wallace et al., 2002). The ages of the uppermost volcanic basement increase southwards from $\leq$ 35 Ma in NKP to $\sim$ 110 Ma on SKP (Duncan, 1991; Coffin et al., 2000). This is because NKP was latterly affected by KP hot spot magmatism (Coffin et al., 2000) (Figure 2.2).

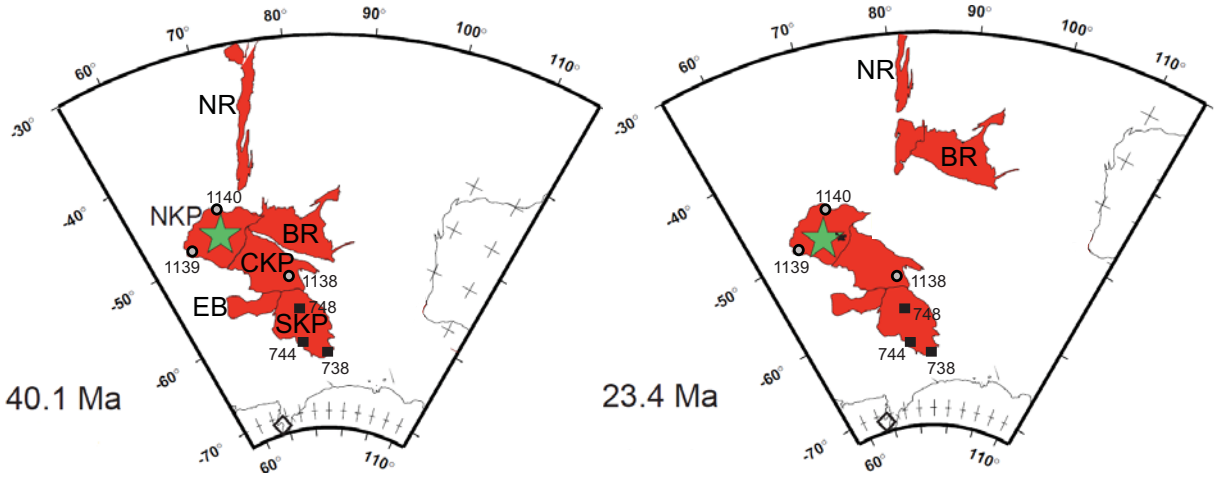

Figure 2.2: The paleogeography of the Kerguelen Plateau - Broken Ridge Large Igneous Province at the Eocene (left) and Oligocene (right) and KP deep-sea drilled sites discussed in this thesis. The star shows the Kerguelen hotspot. The circles represent the location of the sites for which new paleoceanographic records are produced here, and the squares show the sites that will be compared. Modified from Coffin et al. (2000).

2.3 Ocean circulation in the Kerguelen Plateau region

Today the waters of the Antarctic Circumpolar Current (ACC) bathe the entire KP (Figure 2.3). The eastward flowing ACC is the strongest ocean current found in the world and the largest circulation component of today's Southern Ocean (Whitworth, 1988). It is a geostrophic flow (i.e. its pressure is balanced by the Coriolis effect caused by the rotation of the Earth), driven mainly by the westerly winds (Carter et al., 2008). Despite being entirely driven by wind, the ACC extends to the sea bed, where its circulation path is considered to tightly interact with bottom topography (Lazarus and Caulet, 1993) due to the weak stratification and strong barotropicity of the Southern Ocean (Park et al., 2001). As shown in Figure 2.3 the ACC widens to the north and south of the KP limits (Park et al., 1991; 1993; Carter et al., 2008). The relative shallow depths of the KP extending latitudinally over ∼20° on the SO constitute a major barrier to the ACC that steers the flow (Park et al., 2008).

The ACC consists of distinct circumpolar fronts extending from surface to deep-waters, which correspond to water mass boundaries (Orsi et al., 1995). These are narrow oceanic currents that vertically delimit water-masses with different properties (mainly temperature, density and salinity). The ACC fronts are delimited within the constraints imposed by the bathymetry of the KP (Moore et al., 1999). Figure 2.3 depicts the SAF to the north and the southern ACC Front (SACCF) to the south (Orsi et al., 1995). Between these two fronts there is the Antarctic Convergence or Antarctic Polar Front (APF) to the south (Orsi et al., 1995) (Figure 2.4).

The modern path of the APF crosses the latitudes covered in this study of the KP (Figure 2.4). Specifically, the APF lies on average ∼ 50°S (Moore et al., 1999; Park et al., 2008). To its southern edge, colder and denser Antarctic waters converge and sink below warmer less dense sub-Antarctic waters (Moore et al., 1999). Importantly, the APF path

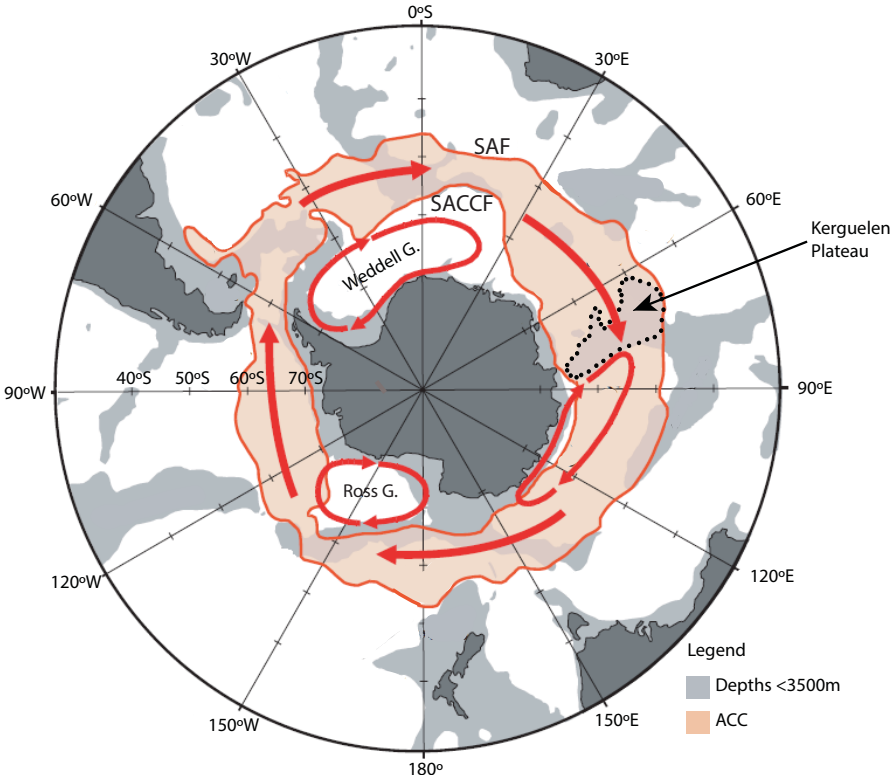

Figure 2.3: General path of the modern Antarctic Circumpolar Current (ACC). It is contained by the Subantarctic Front (SAF) to the north and the southern ACC Front (SACCF) to the south, determined by Orsi et al. (1995). The dotted area depicts the Kerguelen Plateau. Modified from Carter et al. (2008).

around the SO coincides with a belt of elevated primary productivity , and a shift from biocalcareous primary producers and corresponding sedimentary deposits to the north to biosiliceous to the south (Goodell, 1973; Kemp et al., 1975). The shallow component of the APF is separated by the deep part after observed changes in sea surface temperatures by Moore et al. (1999). The shallow part of the APF crosses the KP well south of Kerguelen Island while the main part of its deeper flow is constrained to pass through the north of the plateau (Gille, 1994; Orsi et al., 1995; Barker and Thomas, 2004).

The bathymetry of the KP is complex, specially the NKP and CKP that present several troughs and shoals (Figure 2.5). The NKP and CKP is split from SKP by the Fawn Trough (2650 m water-depth) at 56°S. This regional topography is dominated by two principal current systems borderning NKP and CKP, the deep part of the ACC to the north and the Fawn Trough Current (shallow branch of the ACC) to the south (Park et al., 2008). Both currents merge and flow following the local bathymetry after crossing NKP (east of the plateau) (Park et al., 2008), see Figure 2.5.

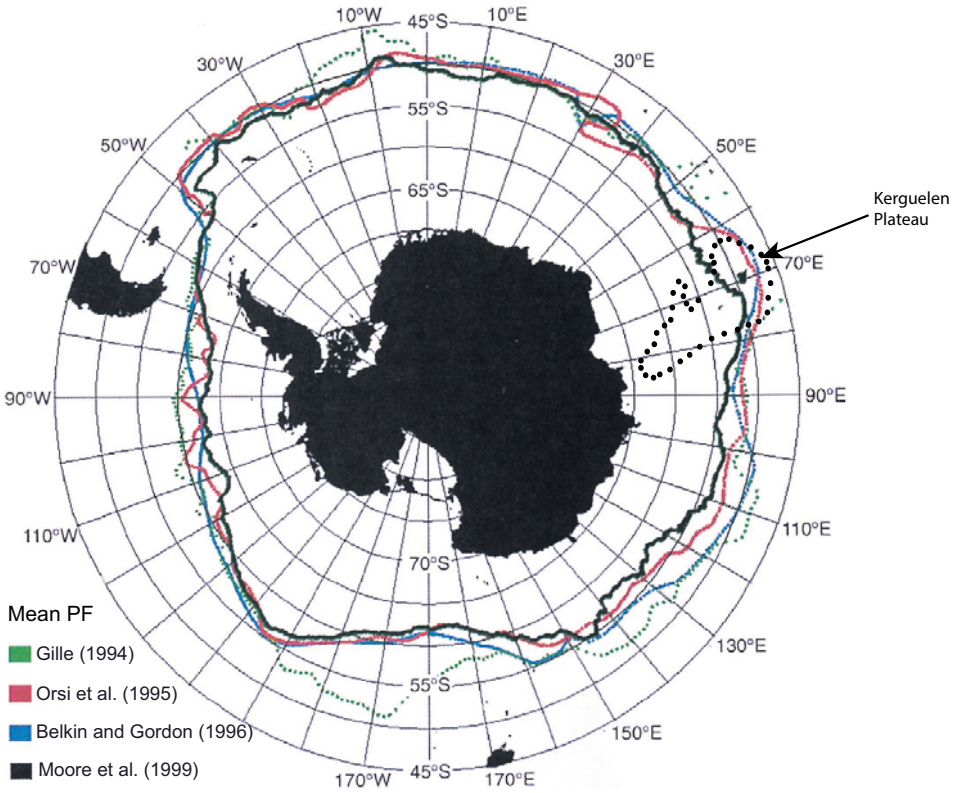

Figure 2.4: Illustration of the calculated modern Polar Front mean track by different studies. The dotted area depicts the Kerguelen Plateau. Modified after Moore et al. (1999).

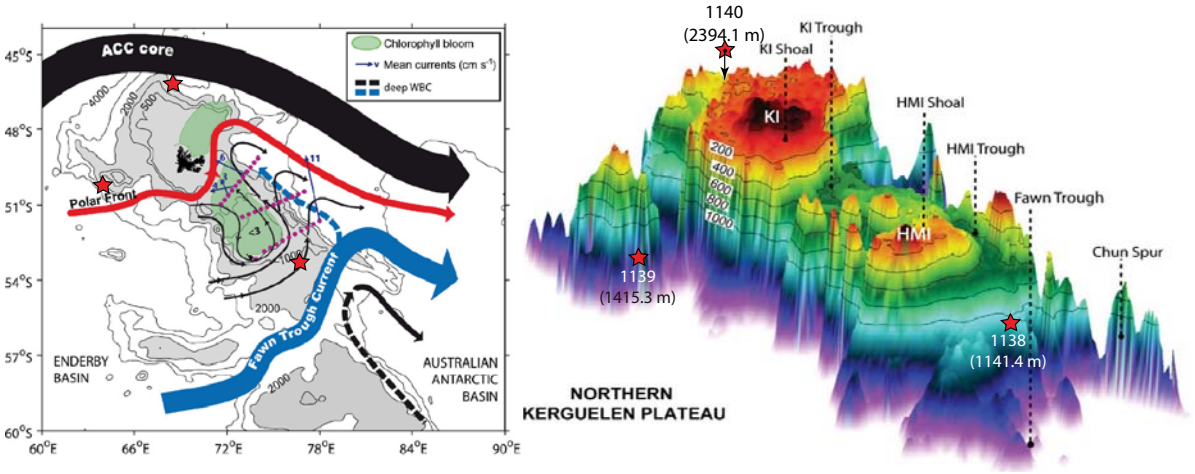

Figure 2.5: Geostrophic circulation over NKP and CKP and seasonal primary productivity blooms (left) and ETOPO2 three-dimensional bathymetry (right) (Park et al., 2008). Stars depict the location of the three study sites and their present day water depths.

2.3.1 View of Southern Ocean circulation at the EOT

Recent model simulations have studied global ocean circulation patterns at the EOT. The models integrate paleogeographic reconstructions, namely the tectonically-active Tasman

Gateway, Drake Passage, Panama Seaway and the Tethys Seaway.

One study showed that the global deep-water cooling at the EOT was led through the deepening of the Tasman Seaway in the presence of an open Drake Passage and associated ACC (Sijp et al., 2011). This was thought to have resulted in a reduction in ocean and atmosphere heat transport from low latitudes , which had helped to keep Antarctica warm in the earlier Paleogene. Another modelling study suggested that the narrowing of the Tethys, the tropical Seaway in the Mediterranean region, was important for EOT climate change (Zhang et al., 2011). This Tethys closure which was on-going through the Paleogene, brought sea surface salinity changes that are likely to be key to the transition from Southern Ocean Deep Water (SODW) to North Atlantic Deep Water (NADW), from which more heat can be transported from surface to deep ocean (Zhang et al., 2011). Lastly, the impact of an opened Panama Seaway which was likely a feature of Eocene-Oligocene times, showed reduced deep water formation in the northern hemisphere from the introduction of warm equatorial waters (Yang et al., 2013). Under these conditions, the SO tends to be relatively saltier than the North Atlantic which enhances deep ocean ventilation at the southern hemisphere (Yang et al., 2013).

2.4 Stable isotopes in foraminifera

Ocean-climate parameters millions of years ago in the Eocene-Oligocene are preserved in the stable oxygen and carbon isotopes of marine $CaCO_3$.

The term stable refers to isotopes of elements that do not undergo radioactive decay whereas the term isotope is attributed to the molecule of a same element that can have different masses. These mass differences are given by a different number of neutrons. Thus, the terminology used of 'light' and 'heavy' isotopes makes reference to the one with less and more neutrons respectively. In addition, the mass differences control the molecular vibration of the respective isotopes. Hence, molecules formed by light isotopes vibrate more than the molecules formed by heavy isotopes leading to weaker bonds in the former and stronger in the latter. As a result, molecules formed from light isotopes react more easily than those from heavy isotopes (Rohling and Cooke, 1999).

The calcium carbonate paleo-thermometer was developed by Urey (1947) since the isotopes fractionate in equilibrium between calcite and water as a function of temperature. He established the $\delta^{18}O$ notation (per mil, ‰) based on the $^{18}O/^{16}O$ ratio. Equation 2.1 shows the notation procedure for getting δ isotope values where R is the ratio ^{13}C /^{12}C for $\delta^{13}C$ and ^{18}O / ^{16}O for $\delta^{18}O$:

$$\delta‰ = [(R_{sample} - R_{std})/R_{std}] \times 1000 \tag{2.1}$$

From Equation 2.1, a positive δ value has an enrichment in the heavy isotope as reference to the standard. On the contrary, a negative δ is depleted in comparison to the reference material.

After Urey's discovery, the first quantitative measurements of temperatures were done in belemnites from the Cretaceous (Urey et al., 1951). This work was followed by Emiliani (1954) who pioneered the use of foraminiferal tests found in deep-sea sediments and applied it to estimate Pleistocene temperatures on glacial-interglacial timescales (Emiliani, 1955).

Two decades after, Shackleton and Opdyke (1973) demonstrated that the $\delta^{18}O$ signal does not only show the temperature of the water in which the tests precipitate. They argued that $\delta^{18}O$ reflects the global ice-volume signal. Hence, it was discovered that the oxygen isotope ratio of sea water is intimately linked with fractionation processes within the hydrological cycle. Shackleton and Opdyke (1973) observed another application of oxygen isotopes. The authors discovered correlations between oxygen isotopes down-core records and magnetostratigraphic data on deep-sea cores. Since both records presented global stratigraphic correlations, it allowed the use of isotope records as a chronological tool, $\delta^{18}O$ - chemostratigraphy. Furthermore, Shackleton (1977) observed downcore $\delta^{13}C$ variations from deep-sea sediment cores and highlighted their use in the study of water mass movement, palaeoproductivity and global organic carbon burial in the deep sea. He also posited the link between terrestrial weathering, carbonate dissolution cycles in deep-sea sediments and the flux of dissolved CO_2 in the oceans from the atmosphere.

It is noteworthy that the ^{18}O and ^{13}C isotopes cannot be accurately determined directly from the sample due to the low percentages that are present in the carbon and oxygen natural elements. Instead, it is necessary to compare the result to a standard carbonate sample of known composition (Rohling and Cooke, 1999).

Both isotope values from benthic foraminifera shells, which is the focus in this study, can be affected by biology-related 'vital-effects' and microhabitat at the sea-floor (Rohling and Cooke, 1999), which must be considered carefully when selecting species for analysis and in interpreting results.

Chapter 3

Drilling on the Kerguelen Plateau

So far 17 sites have been drilled across the Kerguelen Plateau by the Ocean Drilling Program (ODP). Of these, the late Eocene and or early Oligocene sequence useful for paleoceanographic studies was recovered at ten sites (Figures 3.1 and 3.2). In this study I have produced new paleoceanographic data for three sites drilled on Leg 183, ODP Hole 1138A, 1139A and 1140A. Rotary coring and single holes at these sites appear to have discouraged intensive study, however the new paleogeographic coverage offered by these sequences is valuable for ocean climate reconstructions of the impact of ocean climate changes in the SO during the EOT.

Table 3.1 show the main features of the ten EOT sites based on the initial reports from the expedition Leg 119 (Barron et al., 1989), 120 (Schlich et al., 1989) and 183 (Coffin et al., 2000). From North to South these are Sites 1140, 1139, 737, 1138, 747, 1137, 748, 749, 744 and 738; and their E/O core-depth location is shown in Figure 3.2. The figure depicts large depth heterogeneities of the E/O locations that might have resulted from the complex origin and structural evolution of the plateau. There are also represented in Figure 3.2 lithological changes over coring depth at the E/O sites, including the presence of ice-rafted debris (IRD) with an Antarctica source, and preservation of biosiliceous remains (diatoms and radiolarians) that are thought to reflect paleoproductivity increases brought by establishment of nutrient-rich cold deep-waters. On the whole, this shows that the northern KP sites are barren of siliceous microfossils and IRD at the EOT.

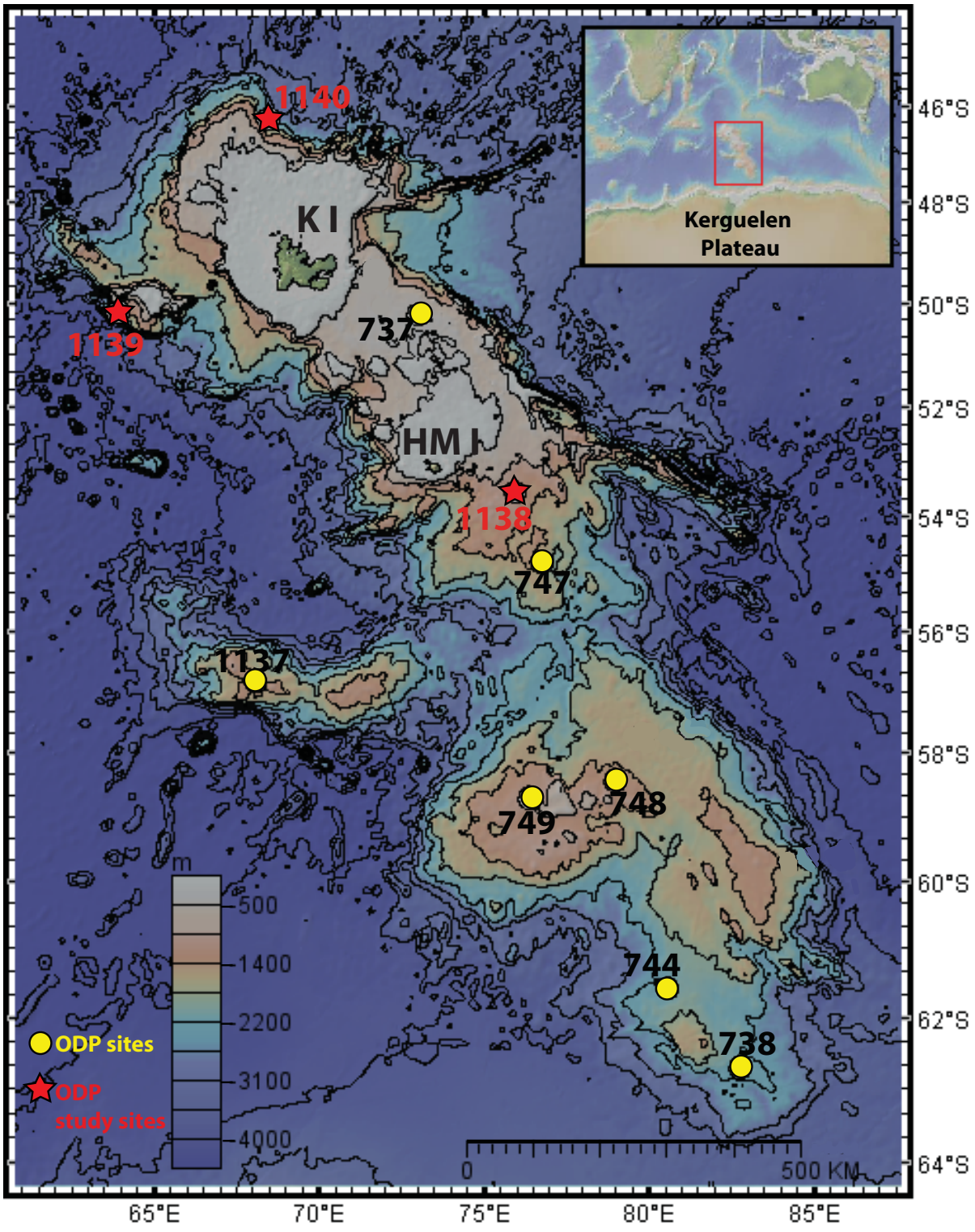

Figure 3.1: Bathymetry of the Kerguelen Plateau showing all ODP sites that contain an Eocene-Oligocene sequence. Red stars identify the three sites which are the focus of this study. KI= Kerguelen Island (Fr.); HMI= Heard and McDonald Islands (UK). Isobath interval= 500m. Basemap generated by GeomapApp software (Ryan et al., 2009).

.

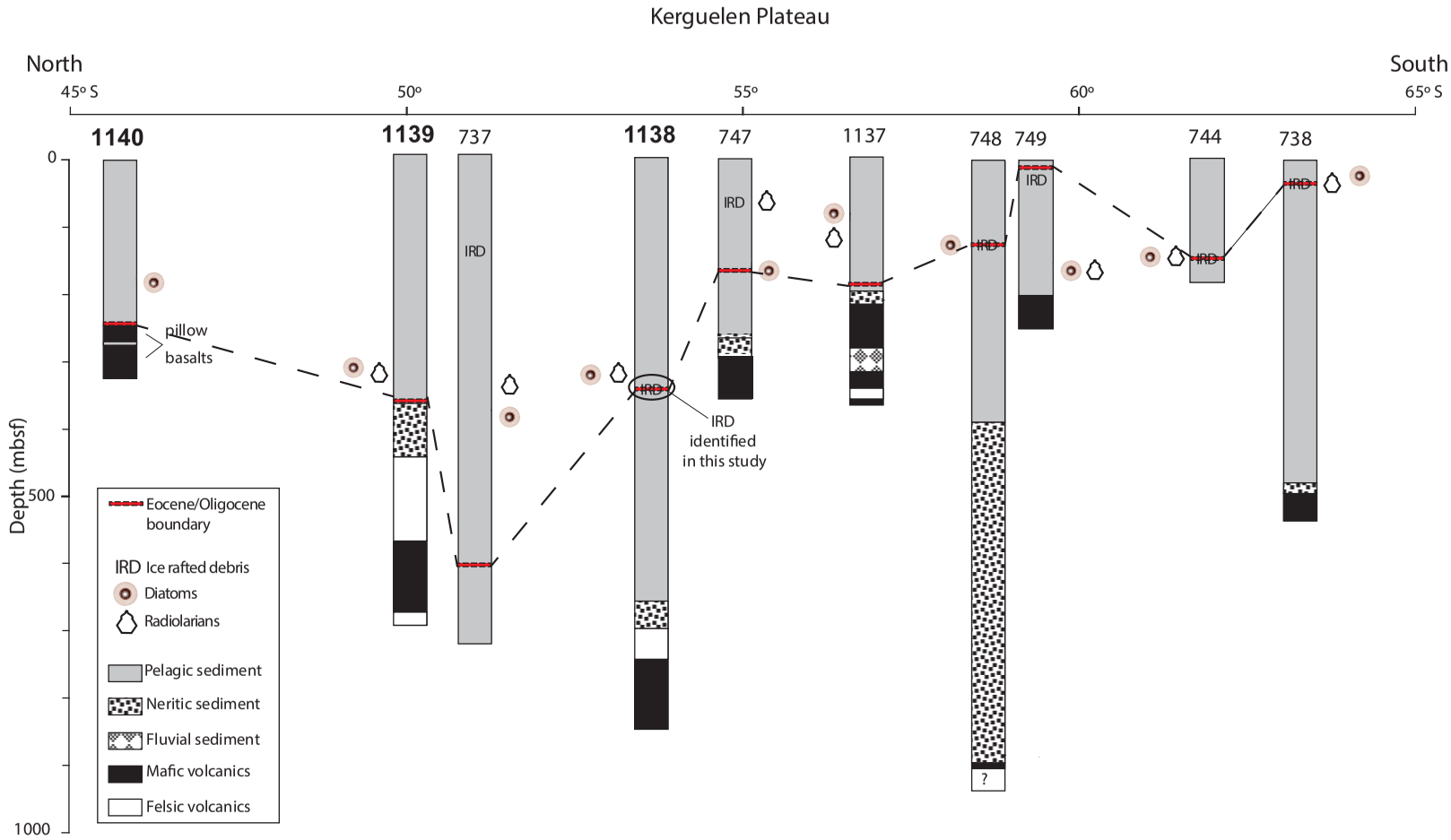

Figure 3.2: Deep sea drill sites cored on the KP in which a late Eocene - early Oligocene sequence was recovered. Also represented are the first appearance of biosilica (diatoms, radiolarians) and ice rafted debris (IRD) based on the initial reports from the respective drilling expeditions (Barron et al., 1989; Schlich et al., 1989; Coffin et al., 2000). Bold font identifies the new sites added in this study.

Site	Modern water depth (m)	Location	E/O recovery (mbsf)	Lithology	Comments
1140	2394	Northernmost KP 46°S 68°E	227.6-270.5	Dolomitized nannofossil chalk interbedded in submarine pillow basalts.	Big age uncertainty due to low sedimentary recovery created by intrusions of pillow basalts. Only site presenting submarine volcanism.
1139	1415	Skiff Bank NW-NKP 50°S, 64°E	383.5	Nannofossil-foraminifera rich chalk.	Lithological change to sandy packstone below the EOT.
737	564	N-CKP 50°S, 73°E	606	Calcareous claystone.	
1138	1141	CKP 53°S, 75°E	383.5	Foraminifer-bearing nannofossil chalk.	Tephra layers of volcanic origin and glauconite filled foraminifera. A hiatus follows the EOT.
747	1695	S-CKP 55°S, 76°E	171	Nannofossil chalk.	
1137	1016	Elan Bank, East of CKP & SKP 56.5°S, 67°E	171.45 - 190.65	Calcareous nannofossil ooze with rare chert nodules.	
748	1291	SKP 58.5°S, 79°E	123.6	Calcareous nannofossil ooze with siliceous debris.	First northernmost evidence of ice-rafted debris at the EOT
749	1070	SKP 59°S, 76°E	15	Calcareous nannofossil and foraminifera ooze with some siliceous microfossils and minor volcanic ash.	
744	2307	S-SKP 61.5°S, 80°E	157.1 - 166.6	Calcareous nannofossil ooze.	
738	2263	Southernmost SKP 63°S, 83°E	35	Calcareous nannofossil ooze	Presence of *Nuttalides umbonifera* might imply initiation of the Antarctic Bottom Water (AABBW)

Table 3.1: Summary of the ten sites at the Kerguelen Plateau (from North to South) containing E/O sections, based on the initial reports from the drilling expeditions (Barron et al., 1989; Schlich et al., 1989; Coffin et al., 2000). Bold font indicates the sites added in this study.

Chapter 4

Materials and Methods

4.1 Sample material

Based on the ODP Leg 183 Initial Reports (Coffin et al., 2000) and the stratigraphic visual core descriptions (see Appendix A, Figures A.1, A.2, A.3), Sites 1138 (CKP), 1139 (Skiff Bank, NKP) and 1140 (NKP) within $\sim 10^{\circ}$ degrees latitude were selected for this study since there has been little subsequent research using the recovered material. The principle objectives of ODP Leg 183 focused on sampling igneous basement cores throughout the KP/Broken Ridge LIP. In consequence, the drilling technique used was the Rotary Core Barrel which is designed for the recovery of oceanic crustal hard rock. From the three sites, a total of 180 sediment samples (20 cm^3 cut piece) were requested from the Kochi Core Center (Japan), where Leg 183 cores are stored. The sediments were recovered from cores 1138A-36R, 1139A-40R, and 1140A-24R & -25R, since the EOT sequences were identified within them from the initial shipboard biostratigraphic work (Coffin et al., 2000). The requested sample spacing was of 10 cm since the aim was to get a moderately-high resolution coverage for the three sites. However, the sample spacings were relocated to avoid sample disturbances and the resulting actual sample spacing was of 5 to 18 cm in Site 1138, 4 to 21 cm in Site 1139, and 4 to 19 cm in Site 1140.

4.1.1 Laboratory sample processing

Since all sediment samples were firm and semi-consolidated they were first hammered in their sealed plastic bags into cm-sized pieces. Approximately 17 cm^3 of the broken pieces were transferred to labelled E-flasks (250 ml) and dried in the oven for a minimum of 24h. The dry mass was recorded using a Sartorius LP 220 S balance (1 mg resolution). Afterwards, 100 ml de-ionized water (DIW) was poured into each E-flask. The conical flasks were sealed with parafilm and shaken on a shaker table *Heildolph UNIMAX 2010* operating at 180 r.p.m. for at least 48 hours. The E-flaks, still sealed, were transferred from the shaking table to an ultrasonic bath. There the samples were ultrasonically shaken in two pulses of 20 seconds each, which has been found to aid cleaning. The next step after the ultrasonic treatment was to separate the sand size fraction from the silt and mud size fractions. To do so, new plastic bags (2-3L) were labelled and introduced into 1L glass beakers lining their walls. A 19 cm diameter sieve 63 μm sieve was then labelled and placed on top of its corresponding beaker, and the wet sample from each E-flask poured onto the

sieve surface. The sample was washed over the mesh using DIW from a spray tank with light-diffusive pressure stream, being careful not to exceed 900 ml filtrate (beaker limit). After this washing cycle the sieves were transferred to the oven and dried at 50°C, whilst the fine fraction was let to settle from suspension in the bag. When the fine material settled, $\sim$ 800 ml of the cleared water was carefully siphoned off using a suction pump. Both the sieves and beakers were introduced into the oven at 50°C in order to dry the coarse and fine fraction. Lastly, the coarse fraction was transferred from the sieve into labelled vials using waxed weigh-paper and a soft brush, and the plastic bags containing the fine fraction were sealed. Both fractions were weighed in their vials and bags to determine percentage size-fraction and sample loss during preparation.

The washing and drying cycles were repeated until the coarse fraction was disaggregated and free of fine material. There were notable differences between the sites in the ease which samples disaggregated. For instance, the samples from site 1139A were the hardest to break up with the hammer. Samples from the intervals 1139A-40R-5, 79 - 81 cm to 1139A-40R-6, 63 - 65 cm contained chalk aggregates even after 2 wash/dry cycles. To separate these aggregates I applied an additional washing method, in which the lumps were introduced into small glass tubes with lid half-filled with DIW. The glass tubes were closed and introduced into the ultrasonic cleaner for 20 seconds. The foraminifera shells were filled with matrix material even after this treatment. In these cases benthic foraminifera were also ultrasonicated individually inside small glass vials filled with DIW to remove matrix material before isotopic analysis.

The dried coarse fraction material was further sorted using a set of sieves with meshes varying from 500 μm to 63 μm. This isolated key size classes of particles aiding the search for benthic foraminifera specimens suitable for isotope analysis. The sieved-sample was poured into a black gridded picking tray, where it was examined using a *Zeiss Stemi 2000* stereoscopic binocular microscope with incident light source. The specimens were picked using a fine sable paintbrush (000) and they were placed in labelled microslides with black background.

To ensure the abundance of benthic foraminifera species, samples from the middle sections of each core (at 75-79 cm) were initially examined. The number of specimens is few but enough for one isotopic analysis on a single sample. After this assessment, I selected *Cibicidoides mundulus* (Brady et al., 1888) (Table 4.1) as a common benthic species thought to have an epifaunal habitat, that is to say living above the sediment-water interface (Jorissen et al., 1995). Based on wall structure and chemistry this species belong to the Order Rotaliida that is characterized by a bilamellar hyaline and perforate wall. Furthermore, this order is characterized by having low Mg calcite and many chambers (10-12 chambers in *Cibicidoides mundulus*). The order is found from the Triassic to Recent. Family: Cibicididae and Genus/species: *Cibicidoides mundulus* (Sen Gupta, 1999). This taxon and its genus has been frequently used for stable isotope studies, and this will allow the comparison among other sites. This species precipitates its test in carbon isotopic equilibrium with seawater, but out of oxygen isotopic equilibrium (0.64‰) (Graham et al., 1981; McCorkle et al., 1990).

Ideally, isotope analysis should be made on monospecific samples (i.e. a single species) from a constant size fraction (i.e. similar ontogenic stages) to overcome the ecological and vital isotope offsets (Rohling and Cooke, 1999). Therefore, I mainly worked within the 150-250 μm size fraction since this typically contained sufficient specimens with the

Cibicidoides mundulus		
umbilical view	**spiral view**	**apertural view**
subcircular	subcircular	bivonvex
involute	evolute	trochospiral
finely perforated wall	coarsely perforated wall	

Table 4.1: Morphological characteristics used in the identification of the benthic foraminifera *Cibicidoides mundulus* used in this study.

best preservation. For the intervals having insufficient specimens in that size class, the range was extended to 250-425 μm. Sufficient specimens were required to achieve a sample weight of $\sim$ 2.0 mg. The number of specimens of*Cibicidoides mundulus* required varied depending on the size class and availability (Appendix B).

4.2 SEM analysis

Before conducting isotope analyses, it is of great importance to assess how well the foraminifera tests are preserved and if there is evidence of diagenetic alteration that might compromise the original shell chemistry. The preservation of large scale test features was general moderate, as seen under the light microscope, however there was evidence for some alteration in the form of mineral overgrowths and recrystallization, specially at certain sites and intervals. Therefore, the preservation was assessed using the Environmental Scanning Electron Microscope (ESEM) Philips XL-30- ESEM-FEG housed at Stockholm University since possible errors may be introduced in the isotopic signal due to diagenesis. In preparation for SEM analysis, 79 specimens from some of the intervals throughout the three sites, and spanning the range of preservational modes were hand picked and mounted on stubs with adhesive surfaces. These stubs were gold coated in order to reduce interference and make them more conductive with the electron beam. The low vacuum mode was used since this minimized charging effects.

4.3 Biostratigraphy and age model

The age-depth model for sites 1138, 1139 and 1140 used here are based on biostratigraphic (planktonic foraminifera and calcareous nannofossil) and magnetostratigraphic age-dating techniques produced by the Leg 183 shipboard science party (Coffin et al., 2000). Planktonic foraminifers zonations were based on Antarctic Paleogene (AP) zonal scheme of Stott and Kennett (1990) modified by Huber (1991), and Berggren (1992). The E/O boundary at high latitudes based on planktonic foraminifera is poorly constrained and has a large error-uncertainty at these high latitude sites since there, planktonic foraminifera diversity is low. This gives less precision of the zonal schemes in the absence of *Hantkenina* spp. The planktonic marker used to approximate the E/O boundary is given by the last appearance datum (LAD) of *Globigerinatheka index* (Coffin et al., 2000). Calcareous nannofossil zonations were adopted from Wise (1983) that were modified by Wei and Wise (1990); and Wei and Thierstein (1991) and calibrated against magnetostratigraphy by Wei (1992)).

The biostratigraphic ages (Figure 5.4) were calibrated against the magnetic polarity time scale of Cande and Kent (1995). Therefore, all presented numerical ages in this study are relative to it.

4.4 Stable oxygen and carbon isotope analyses in benthic foraminifera

Stable isotope measurements from the 180 samples were performed on the Gasbench II - MAT253 mass spectrometer hosted at Stockholm University. The major components of this mass spectrometer are (1) the analyser, consisting of an ion source, a flight tube and a collector system; (2) a differential pumping system, to maintain a vacuum within the analyser for reducing molecular air collisions that would result as a loss of charge in the ions.

For each sample, an average of 16 specimens from the 150-250 μm size fraction were transferred from the microslides into disposable silver boats (6 x 6 x 12 mm) using a 000 paintbrush. These silver containers were placed on a Sartorius MC5 microbalance (0.001 mg resolution) using lab tweezers and were weighed adding specimens until the standard mass of $\sim$ 0.2 mg was reached. The weights and number of specimens picked are shown in tables in Appendix B. As shown in this table, the mass from Sites 1139 and 1140 was not always enough due to the lack of enough *Cibicidoides mundulus* specimens. This precluded the isotope analysis with the standard mass of 0.2 mg, and half of the mass was used instead (ranging from 0.05 to 0.1 mg). After weighing, the foraminifera in the silver containers were poured into screw cap Labco glass vials screw capped with a volume of 12 ml for 0.2 mg mass and 5.9 ml for the 0.1 mg samples. The lid was labelled with the sample ID and the vials were in the oven drying for 24 hours at 60°C.

According to the Gasbench II methods, prior to the spectrometric analysis, the foraminifera samples must be reacted to generate carbon dioxide (CO_2) gas offline. To do so, the vials were opened and inclined horizontally and 100 μl H_3PO_4 of 99.6% was carefully added on the vial's wall without touching the sample. While still horizontal, the vials were closed and flushed with Helium gas (100 ml/min) for 10 minutes to remove gas ambient including water vapour. The vials were then returned to a vertical position to allow the sample react with the phosphoric acid overnight. The CO_2 produced from the reaction of carbonate with phosphoric acid follows Equation 4.1.

$$CaCO_3 + H_3PO_4 \Leftrightarrow CaHPO_4 + CO_2 + H_2O \tag{4.1}$$

The mass spectrometer compares the mass ratios of CO_2 obtained from the sample, with reference to a CO_2 reference standard of known composition. This standard is needed since it is calibrated against the reference gas (a gas that is calibrated against the carbonate standard) which the mass spectrometer runs at the beginning and end of each sample analysis. Here, we will report the final isotopic ratios using the international standard Vienna Pee Dee Belemnite (VPDB) marine carbonate. By definition, the $\delta^{18}O$ and $\delta^{13}C$ from VPDB are equal to zero (Epstein et al., 1953). Actual VPDB material is no longer available. Instead, a standard calibrate through intercomparison with VPDB was used, termed IAEA-CO-1 calcite material. IAEA-CO-1 differs by +2.492 in $\delta^{13}C_{VPDB}$ (standard deviation = 0.030) and by -2.4 $\delta^{18}O_{VPDB}$ (standard deviation = 0.1) (Stichler, 1995). Thus,

the same procedure was applied to the IAEA-CO-1 calcite. Twenty vials containing 0.2 mg of powdered IAEA-CO-1 calcite were also weighed and reacted with the phosphoric acid.

Finally, standard and geologic samples were placed into the mass spectrometer autosampler for analysis. The analytical precision applied is one measurement of the standard to ten measurements of foraminifera samples. Inside the mass spectrometer, the ions are accelerated by electrostatic potential until they reach the magnet. After passing through the magnetic field, the flow of ions are sorted by a particular mass/charge ratio which produces a 'physical fractionation' where the heavier isotope beams will bend less than the lighter ones. For CO_2, the isotopes collected are of masses 44, 45, and 46 amu. The ion beam travels until it arrives into Faraday collectors where the input is converted into an electrical impulse. Therefore, the output signal is a voltage corresponding to the abundance of different carbon and oxygen isotopic ratios. The 46/44 ratio of the current is calibrated in reference to the VPDB using the software Isobat that controls the mass spectrometer. Finally, the stable isotope ratio data is reported using standard delta notation (δ) as the ‰ difference relative VPDB.

Chapter 5

Results

5.1 Deep-sea sediment samples

The results are based on the investigation of 180 deep-sea sediment samples. At each site, the samples were examined down-core to record variations in sediment lithology and colour.

Forty-seven samples were studied at Site 1138, ranging from 1138A-36R-2, 75.0-79.0 cm to 1138A-36R-CC. The sediment samples consist of friable nannofossil chalk. The colour turns from very light greenish grey to white downcore (from section 5 and throughout section 6), and it is not homogeneous since whitish mottling is common indicating bioturbation. The samples are burrow-filled by a whiter sediment downcore from section 5 and throughout section 6. Scattered dark particles are found in all samples.

Sixty-nine samples were analyzed at Site 1139, from 1139A-40R-1, 63-65 cm to 1139A-40R-CC. The samples consist of dark grey friable chalk. Some samples contain mm-scale lighter greenish-grey bands, and pink, orange, brownish stains. Almost all samples show burrows that are filled by dark particles. The most remarkable feature is that the colour of the sediment changes dramatically with a grey to a reddish orange downcore into section 5.

Sixty-five samples were investigated at Site 1140. These extend from 1140A-24R-5, 42-44 cm to 1140A-25R-CC. The samples consist of friable chalk that is beige in color. There is a gradual switch from pale beige to pale brown colour down-core. There are a few burrows filled by whiter sediment that become larger with increasing depth. Some samples contain yellowish-green laminations and black particles. Brown scattered particles exist only in the last sections.

5.2 SEM analysis

Three plates showing the preservation of *Cibicidoides mundulus* (Plate 1 - Site 1138, Plate 2 - Site 1139, and Plate 3 - Site 1140) are presented and described.

Generally, the benthic foraminifera analysis were moderately well preserved, however there is great variability between sites and with different core depths. The species of *Cibicidoides mundulus* has a porous wall making it more prone to degradation. Most specimens are affected by dissolution, this takes the form of corroded by nannofossil contact

dissolution and roughness to the surface texture. This os not a serious issue to isotopic analysis since only a small amount of material is removed. Also visible under the SEM are diagenetic subeuhedral glauconite overgrowths (Plate 1 and 2), and recrystallization by euhedral crystals of dolomite (Plate 3). This could present a bigger problem to isotopic analysis. Fragmented tests were more prone to degradation and therefore avoided for isotope analysis. The inside of the tests that were crushed on stub show good preservation. Test wall cross-sections also generally look intact, with no evidence for growth of large, angular secondary crystals.

5.2.1 Plate 1 - Site 1138

Plate 1 is ordered downcore by view type of the *Cibicidoides mundulus*: (1-5) spiral side, (6) fragment, (7-9) tests crushed on stub, (10-12) umbilical side.

(1) Dissolution preferentially starts on the spiral perforation nature of the species leaving larger holes 183-1138A-36R-2, 103-105 cm; (scale bar= 100 μm); (1a) close-up showing the imprint of calcareous nannofossil signalling 'contact' dissolution (scale bar= 10 μm); (1b) close-up through a pore, the inside wall shows recrystallization by subeuhedral crystals (scale bar= 10 μm). (2) 183-1138A-36R-3, 36.5-38.5 cm; (scale bar= 100 μm); (2a) & (2b) whole nannofossils trapped in pores, but their small size does not affect the dominant stable isotope signature (scale bar= 5 μm). (3) Degradation of the ultimate chamber by dissolution 183-1138A-36R-3, 36.5-38.5 cm (scale bar=100 μm). (4) Glauconite overgrowth masks the original wall porosity; 183-1138A-36R-3, 147-149 cm (scale bar=100 μm). (5) Degradation of the wall in two chambers showing glauconite filling; 183-1138A-36R-4, 3-5 cm (scale bar=100 μm). (6) Fragment showing recrystallization by subhedral crystals; 183-1138A-36R-5, 3-5 cm (scale bar=50 μm). (7) Good preservation of the inside wall; 183-1138A-36R-2, 103-105 cm (scale bar=20 μm). (8) Good preservation of the test's cross-section and chamber interior; 183-1138A-36R-3, 36.5-38.5 cm (scale bar=20 μm). (9) No visible diagenetic overgrowth of test's interior; 183-1138A-36R-4, 15-17 cm (scale bar=20 μm). (10) Nannofossil contact dissolution; 183-1138A-36R-2, 103-105 cm (scale bar=100 μm). (11) Last chamber shows a diagenetic overgrowth; 183-1138A-36R-5, 3-5 cm (scale bar=100 μm). (12) Nannofossil contact dissolution and dissolution holes; 183-1138A-36R-6, 14-16 cm (scale bar=100 μm).

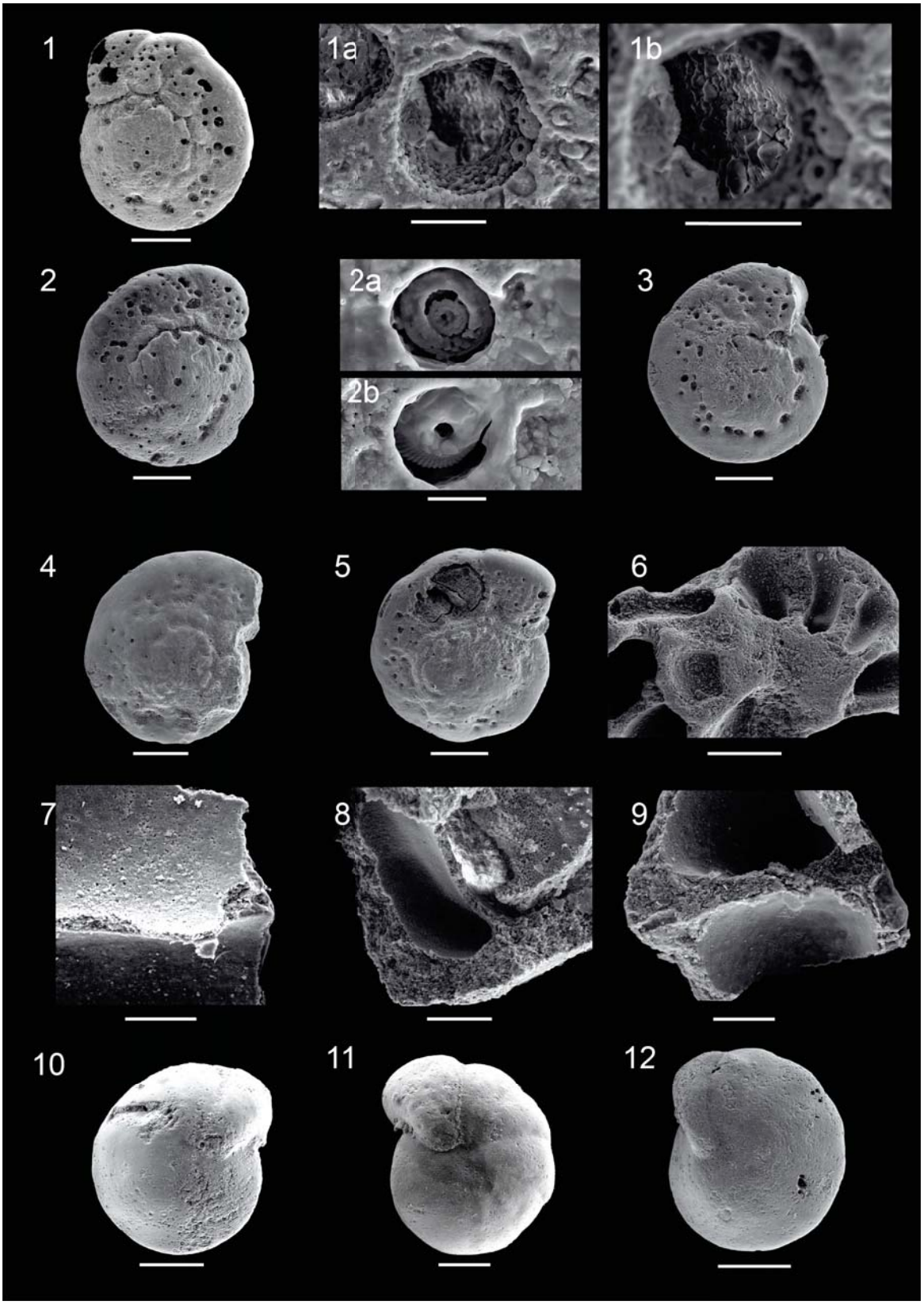

Plate 1 - Scanning electron microscope images of benthic foraminifera *C. mundulus* from the EOT sequence of ODP Site 1138.

5.2.2 Plate 2 - Site 1139

Plate 2 is organized by view type downcore: (1-8) spiral view, (9) fragment, (10-18a) umbilical view. The specimens of *C. mundulus* from Site 1139 generally are less well preserved than the Site 1138, but some show moderate preservation.

(1) Test degradation by dissolution starts inside the test natural porosity; 183-1139A-40R-1, 63-65 cm (scale bar= 100 μm). (2) Corrosion of the test; 183-1139A-40R-1, 78-80 cm (scale bar= 100 μm). (3) Dissolution and loss of the two last chambers; 183-1139A-40R-2, 135-137 cm (scale bar= 100 μm); (3a) close-up showing dissolution of the test pores, and slightly recrystallization on the wall (scale bar= 10 μm). (4) Mineral overgrowth in the right side of the test; 183-1139A-40R-4, 98.5-100.5 cm (scale bar= 300 μm). (5) Ultimate chamber shows 'peeling-off' of its outer layer and a lithified filling; 183-1139A-40R-5, 111-113 cm (scale bar= 100 μm). (6) Mineral overgrowth on the test; 183-1139A-40R-5, 147-149 cm (scale bar= 100 μm); (6a) pore close-up showing diagenetic overgrowth (scale bar= 5 μm). (7) Chamber loss by corrosion and dissolution and mineral overgrowth masking the wall's porosity; 183-1139A-40R-6, 39.5-41.5 cm (scale bar= 100 μm). (8) Fragmented shell highly recrystallized; 183-1139A-40R-4, 98.5-100.5 (scale bar= 100 μm). (9) Corrosion of the outer wall layer showing recrystallization of the interlocular chambers; 183-1139A-40R-1, 78-80 cm (scale bar= 100 μm); (10) Corrosion and dissolution with wall loss; 183-1139A-40R-2, 135-137 cm (scale bar= 100 μm). (11) Nannofossil corrosion and recrystallization is visible inside the ultimate chamber; 183-1139A-40R-2, 135-137 cm (scale bar= 100 μm). (12) Corrosion and wall loss, large holes; 183-1139A-40R-2, 135-137 cm (scale bar= 100 μm). (13) Dissolution wall loss. Interlocular chambers show relief. Dissolution holes; 183-1139A-40R-4, 98.5-100.5 cm (scale bar= 100 μm). (14) Mineral overgrowth and large holes affects the original test; 183-1139A-40R-4, 98.5-100.5 cm (scale bar= 200 μm). (15) Good preservation of the porous wall and degradation of the last chamber; 183-1138A-40R-5, 101-103 cm (scale bar= 300 μm); (15a) close-up revealing recrystallization on the wall and around the pores (scale bar= 20 μm). (16) Corrosion of the outer wall, large holes and ridges 183-1139A-40R-5, 135-137 cm (scale bar= 100 μm). (17) Degradation of the ultimate chamber and mineral overgrowth on the wall; 183-1139A-40R-6, 90-92 cm (scale bar= 100 μm); (17a) close-up showing recrystallization (scale bar= 30 μm).

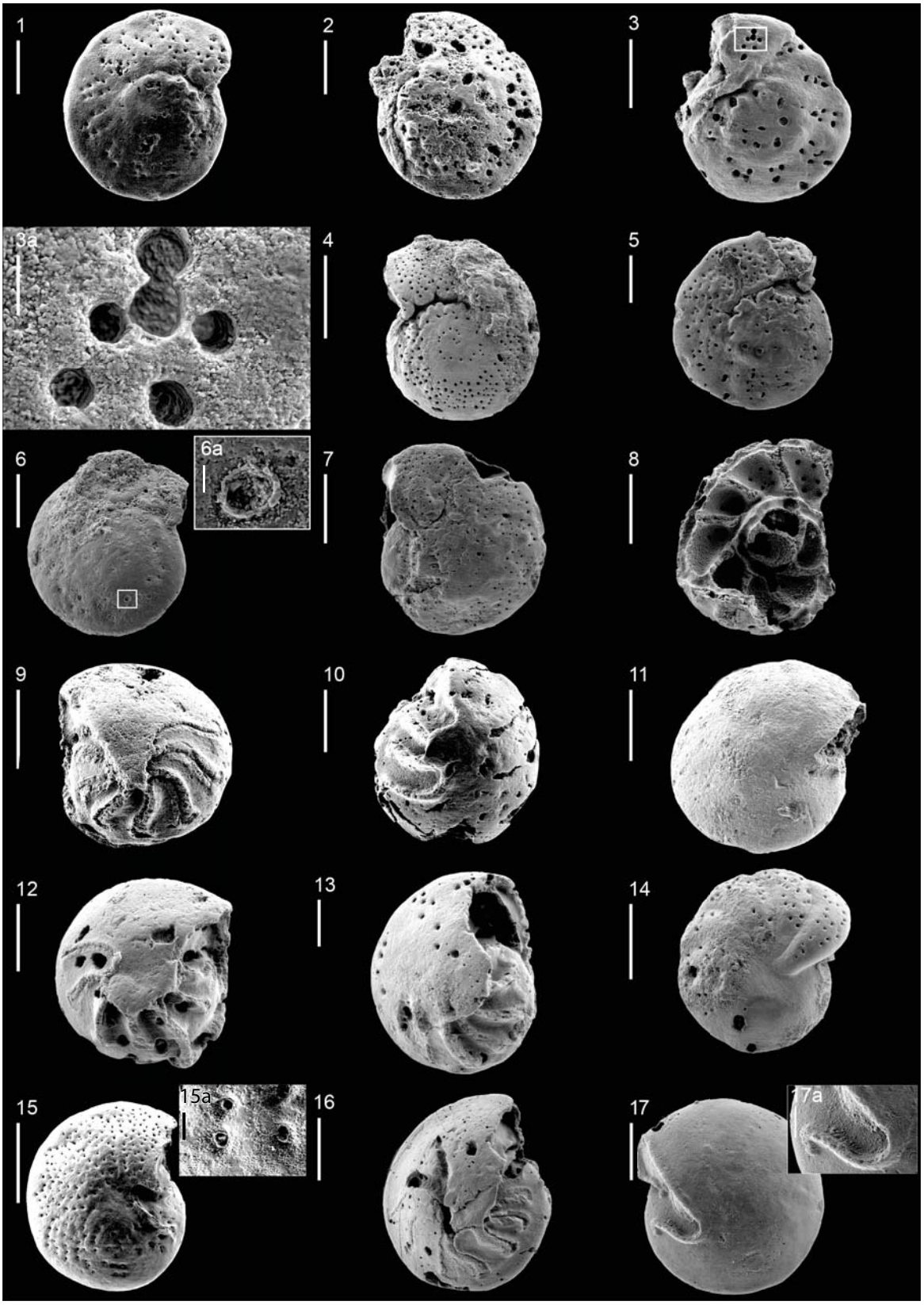

Plate 2 - Scanning electron microscope images of benthic foraminifera *C. mundulus* from the EOT sequence of ODP Site 1139.

5.2.3 Plate 3 - Site 1140

Plate 3 shows *C. mundulus* micrographs ordered downcore by type view: (1-9a) spiral view; (10-14) umbilical view.

(1) Ultimate chamber loss and contact dissolution; 183-1140A-24R-5, 42-44 cm (scale bar= 100 μm). (2) Euhedral dolomite crystal growing in the ultimate chamber; 183-1140A-25R-1, 18-20 cm (scale bar= 100 μm). (3) Dolomite euhedral crystals growing in the holes of the test;183-1140A-25R-1, 18-20 cm (scale bar= 100 μm); (3a) Close-up showing dolomite euhedral crystals and contact dissolution (scale bar= 40 μm). (4) Planktonic foraminifera contact dissolution; 183-1140A-25R-1, 18-20 (scale bar= 30 μm). (5) Euheral dolomite crystal growing on the wall and last chamber loss; 183-1140A-25R-3, 118-120 cm (scale bar= 100 μm). (6) Close-up showing an euhedral crystal growing inside a pore; 183-1140A-25R-4, 84-86 cm (scale bar= 10 μm). (7) Recrystallization of the wall and pore, and corrosion of the wall; 183-1140A-25R-4, 146-148 cm (scale bar= 10 μm). (8) Recrystallization of euheral dolomite replaces the test; 183-1140A-25R-4, 146-148 cm (scale bar= 100 μm). (9) Dolomite recrystallization in the ultimate chamber; 183-1140A-25R-5, 71-73 cm (scale bar= 100 μm). (10) Dolomite replacing the wall and degradation of the last chambers; 183-1140A-25-R1, 65-67 cm (scale bar= 100 μm). (11) Ultimate chamber loss and mineral overgrowth; 183-1140A-25R-3, 118-120 cm (scale bar= 100 μm). (12) Nannofossil contact dissolution; 183-1140A-25R-4, 16-18 cm (scale bar= 50 μm). (13) Chamber loss and contact dissolution; 183-1140A-25R-4, 16-18 cm (scale bar= 100 μm); (13a) close-up showing recrystallization on the wall (scale bar= 10 μm). (14) Dolomite recrystallization and degradation of the last chambers; 183-1140A-25R-5, 71-73 cm (scale bar= 100 μm).

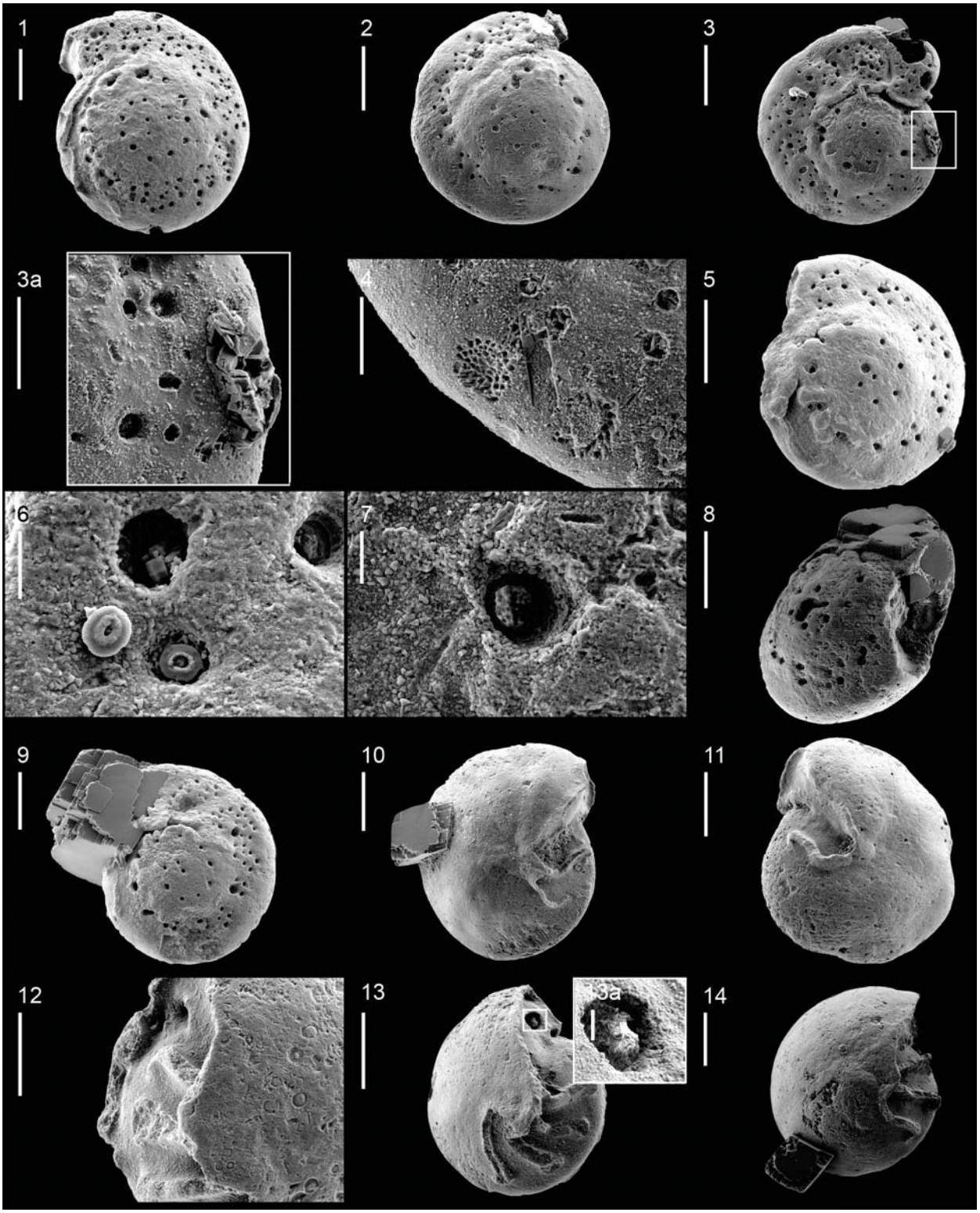

Plate 3 - Scanning electron microscope images of benthic foraminifera *C. mundulus* from the EOT sequence of ODP Site 1140.

5.3 Stable isotope records and Sand Fraction characteristics

The new δ^{18}O and δ^{13}C data from *C. mundulus* at Sites 1138, 1139, and 1140 is given in Appendix B. The carbon and oxygen records were initially plotted against depth (Figures 5.1, 5.2, and 5.3) to see if they could provide independent chemostratigraphies for the respective sites. In terms of statistic analysis of the data, it was generally not possible to do replicate analysis on a single sample because there were too few specimens, usually all sampled. However, each isotopic analysis was made on multiple specimens, $\sim$ 16 on average (Appendix B), which minimizes variability between specimens, thereby increasing the potential for a reproducible value.

The coarse fraction holds the microfossil components and therefore was the one investigated in this study. Foraminiferal preservation and *Cibicidoides mundulus* availability in each sample was evaluated by visual estimations at all samples. The proportion of coarse fraction against depth is shown in Figures 5.1, 5.2, 5.3 together with the isotope values.

5.3.1 Site 1138

The new isotope records for Site 1138 present a distinctive increase across the shaded interval shown in Figure 5.1, $\sim$ 1.2‰ increase in δ^{18}O and $\sim$ 1‰ increase in δ^{13}C from $\sim$ 340.5 - 338.5 mbsf. It is proposed that this isotope increase correlates to the characteristic EOT isotope shift (Zachos et al., 1999; Coxall and Pearson, 2007; Coxall and Wilson, 2011) (see Figure 2.1 on page 8 of this thesis). This is superimposed on smaller scale fluctuations over $\sim$ 50 cm intervals with δ^{18}O varying by $\sim$ 0.3‰ and δ^{13}C by $\sim$ 0.4‰.

Visual inspections of the curves suggest that variability in both isotope signals correlated in almost all the step-shifts in the lower-to-middle part of the curve. The lowest part of the plot (340.6 - 340.025 mbsf) shows a $\sim$ 20 cm lag of the δ^{13}C with respect of δ^{18}O. Towards the middle of the sequence, between 338.5 - 337.5 mbsf, δ^{13}C appears to lead δ^{18}O; and above, both records vary independently.

There is a peak in δ^{18}O and δ^{13}C around 338 - 338.5 mbsf, with values reaching $\sim$ 1.9‰ and $\sim$ 1.45‰ respectively. Thereafter, both systematically decrease up-section to mean values of $\sim$ 1.1‰ in δ^{18}O, and $\sim$ 0.9‰ in δ^{13}C between $\sim 337 - 335.25$ mbsf.

The δ^{18}O values within 337.53 - 337.36 mbsf showed a pronounced change that was not recorded in δ^{13}C. This suggests that the δ^{18}O value might be biased. Besides, the isotope spikes in Site 1138 at 337.02 mbsf , and 337.53 mbsf might be diagenetic signals since they correspond to intervals of poorer calcite preservation and extensive glauconitization of the specimens (see in Plate 1, figures 4 and 5). Both of the aforementioned analysis were repeated, still giving extreme values.

Site 1138 sand fraction

Weight % coarse fraction as well as qualitative assessments of foraminifera dissolution, foraminifera abundance, glauconite overgrowths and lithics abundance are shown in Figure 5.1.

In all studied samples from this site planktonic foraminifera species dominate over benthics. In general, however, benthic species are relatively abundant at the sites studied

compared to many other deep ocean sites. They actually dominate the assemblages in the 500-355 μm size fraction. Exceptionally large examples ($> 500\mu m$) of one single benthic species appear in at least one interval at each section.

Within the 250-150 μm the dominant benthic species from the *Cibicidoides* genus was *C. mundulus*. Other minor biogenic components included ostracods (common between the 500-355 μm size fraction), echinoid remains, and fish teeth. These components suggest relatively high benthic food availability. Scattered granite clasts appeared in the $> 425\mu m$ size fraction up in the studied sections that might indicate ice rafted debris (IRD) due to the proximity of Heard and McDonald Islands.

Overall, preservation of benthic foraminifera was better than that of planktonic foraminifera, since the latter have dissolution holes on their test walls. This is consistent with Arrhenius (1952); Berger (1973) observations that planktonic foraminifera were more prone to dissolution than benthic foraminifera. Nevertheless, benthic foraminifera primarily from the *Cibicidoides* genus had lost their ultimate chamber (e.g. Plate 1, specimen 3) a first sign of dissolution that attacks thin, calcite layers of the last formed chambers.

The $63-150\mu m$ size fraction consisted mainly of foraminiferal shell fragments. Microfossil preservation deteriorates up-section. Despite this decline in foraminiferal preservation, no silica microfossils were found throughout the studied intervals. Diatoms were recorded in the Oligocene in Shipboard reports Coffin et al. (2000), however these would not be present in the coarse fraction studied here because of their small size. A second feature that coincides with deteriorating preservation was the presence of the mineral glauconite that often occurred as grains from casts of planktonic tests. Some benthic species also showed the last chamber filled by glauconite 5.1. The percentages of glauconitic tests change from 20% to 5% down section. The presence of glauconite creates the characteristic greenish color of the sediment-samples. Glauconite is an authigenic mineral composed of hydrated iron-rich micaceous clay minerals of the illite group (Rothwell, 1989). This clay assemblage was related to presence of ice sheets on Antarctica in the early Oligocene (Ehrmann and Mackensen, 1992; Salamy and Zachos, 1999). Glauconite formation requires high supply of Fe and K, a suitable redox potential facilitated by the presence of decaying organic matter, and relatively low sedimentation rates to allow the glauconitisation process happen by reactions with seawater on the sea floor (Cloud, 1955; Rothwell, 1989). This is in accord with the low sedimentation rates of Site 1138 (10.1 m/Ma).

Weight % coarse fraction. The samples from Site 1138 provided the highest percentages of coarse fraction among the three new sites studied ranging from $\sim 8 - 40\%$.

There is a prominent increase of $\sim$ 30 % in coarse fraction up-section at 338.5 mbsf (sample 1138A-36R-4, 102 - 104 cm) consistent with a rise in the planktonic foraminifera content. In addition, this shift in higher weight % coarse fraction is simultaneous with the isotope peaks of oxygen and carbon, and with increases in glauconite and benthic foraminifera. Afterwards, these increase is mantained and the samples showed a larger number of infaunal benthic species (benthic species that live partly buried in the soft sediment) that are related to higher productivity levels.

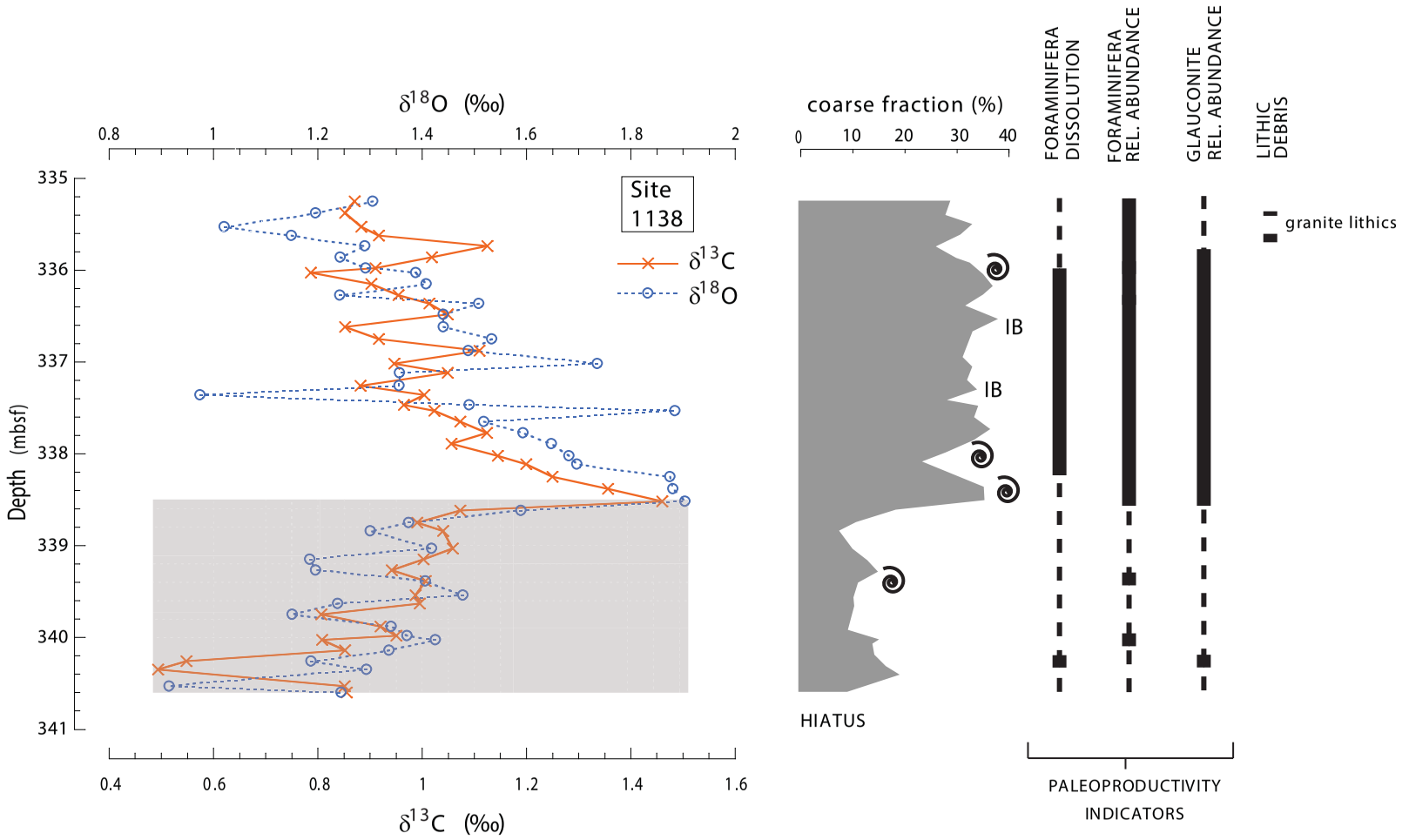

Figure 5.1: Site 1138 benthic foraminifera *C. mundulus* δ^{13}C and δ^{18}O records produced in this study plotted against depth and compared to coarse fraction weight %, foraminifera preservation and lithologic assessments. The shaded area identifies a $\sim$ 1.2‰ increase in δ^{18}O and $\sim$ 1‰ increase in δ^{13}C from $\sim$ 340.5 - 338.5 mbsf that I interpret as corresponding to the global isotopic increase characteristic of the EOT (Figure 2.1). (Spirals: occurrence of unusually large benthic foraminifera specimens ($> 500\mu m$), IB: infaunal benthic (i.e. *Uvigerina* spp. and unilocular forms).

5.3.2 Site 1139

The new Site 1139 *C. mundulus* isotope values show a distinctive isotopic increase of 1.0 ‰ in δ^{18}O and 0.4 ‰ in δ^{13}C in the lower part of the sequence, between 382.32 - 382.05 mbsf (shaded area in Figure 5.2). The δ^{18}O signal continues with high values whilst δ^{13}C recover to lighter values. Up in the sequence follows large scale fluctuations of 0.7 ‰ over $\sim$ 1 m intervals in δ^{18}O and of 0.4 ‰ over $\sim$ 75 m intervals in δ^{13}C. This large δ^{18}O variability visually shows that both isotope signals are not in phase throughout the represented sequence. Overall, the Site 1139 isotope values are lighter for both δ^{18}O and δ^{13}C in comparison to Site 1138 and 1140. A negative value was reached at 376 mbsf for δ^{18}O.

Site 1139 sand fraction

Weight % coarse fraction as well as qualitative assessments of foraminifera preservation, foraminifera abundance, glauconite and lithics presence are shown in Figure 5.2.

The sediment samples from Site 1139 come from the deepest part of the core ($\sim 380m$) of all sites studied. Unusually large benthic foraminifera were retrieved in some sample intervals throughout the studied sequence (spirals in Figure 5.2). Volcanic clasts, basalts and plutonic rock fragments diluted the biogenic components in the samples from the upper intervals of core 1139-40R. The debris gave the chalk a dark grey color. The high content of volcanic debris is in accordance with the proximity of Site 1139 to Skiff Bank, a now submerged volcano(Reusch, 2002). Therefore, the samples contain little biogenic material. Ostracods, infaunal benthics and epifaunal benthics are present. Planktonic foraminifera make up more than the 50% of the total biogenic components. Mineral debris and forminiferal fragments are abundant within the $63 - 150\mu m$ size fraction. Euhedral magnetite crystals in the $150 - 250\mu m$ size fraction were observed in samples 1139A-40R-3, 144-146 cm; 1139A-40R-5, 3-5 cm and 1139A-40R-5, 123-125 cm. It is noteworthy that a 4 mm-sized quartz was found at the last interval of section 1139-40R-6, 90-92 cm (382.2 mbsf).

This site presents the poorest preserved samples of all sites (Plate 2). The foraminiferal preservation decreases downcore. This started from sample 1139A-40R-5, 79 - 81 cm where the planktonic foraminifera became filled by pinkish nannofossil chalk sediment. At this interval there was also presence of glauconite, that occurred both as aggregates and infilling foraminiferal tests. The glauconite aggregates did not break down, even after several washing cycles and they showed a rusty brown colour change downcore suggesting oxidation. Because of the low biogenic content and poor carbonate preservation 23 out of 69 samples had insufficient *C. mundulus* specimens for stable isotope analyses. Therefore, I used half of the standard mass (0.1 mg) for their isotopic analysis which slightly increases the standard error of the results at Site 1139. The coarse fraction proportion appears to fluctuate together with δ^{18}O in the deepest part of the sequence. The shaded isotopic shift (Figure 5.2) begins with a distinct peak in sand fraction at $\sim$ 378 mbsf followed by a minimum plateau and then increases up in the sections.

Weight % coarse fraction. The weight % sand fraction varies between 21.5% and 1.8%. There is an increase in coarse fraction of 13.7% in sample 1139A-40R-3, 121 - 123 cm (378.01 mbsf). Microscope examination reveals that this sample has higher microfossil

diversity, bigger *C. mundulus* specimens, higher content of volcanics and more glauconite lumps. This interval of higher % coarse fraction is present until reaching a second peak in sample 1139A-40R-4, 29 - 31 cm. Then, up-section follows a fewer number epifaunal benthic and infaunal benthic content that are poorly preserved.

During sample sieving, the fine fraction (<63 μm) component of all samples took an unusually long time to settle (5 days). Layers of dark particles deposited horizontally in the beaker when they sink after each washing cycle.

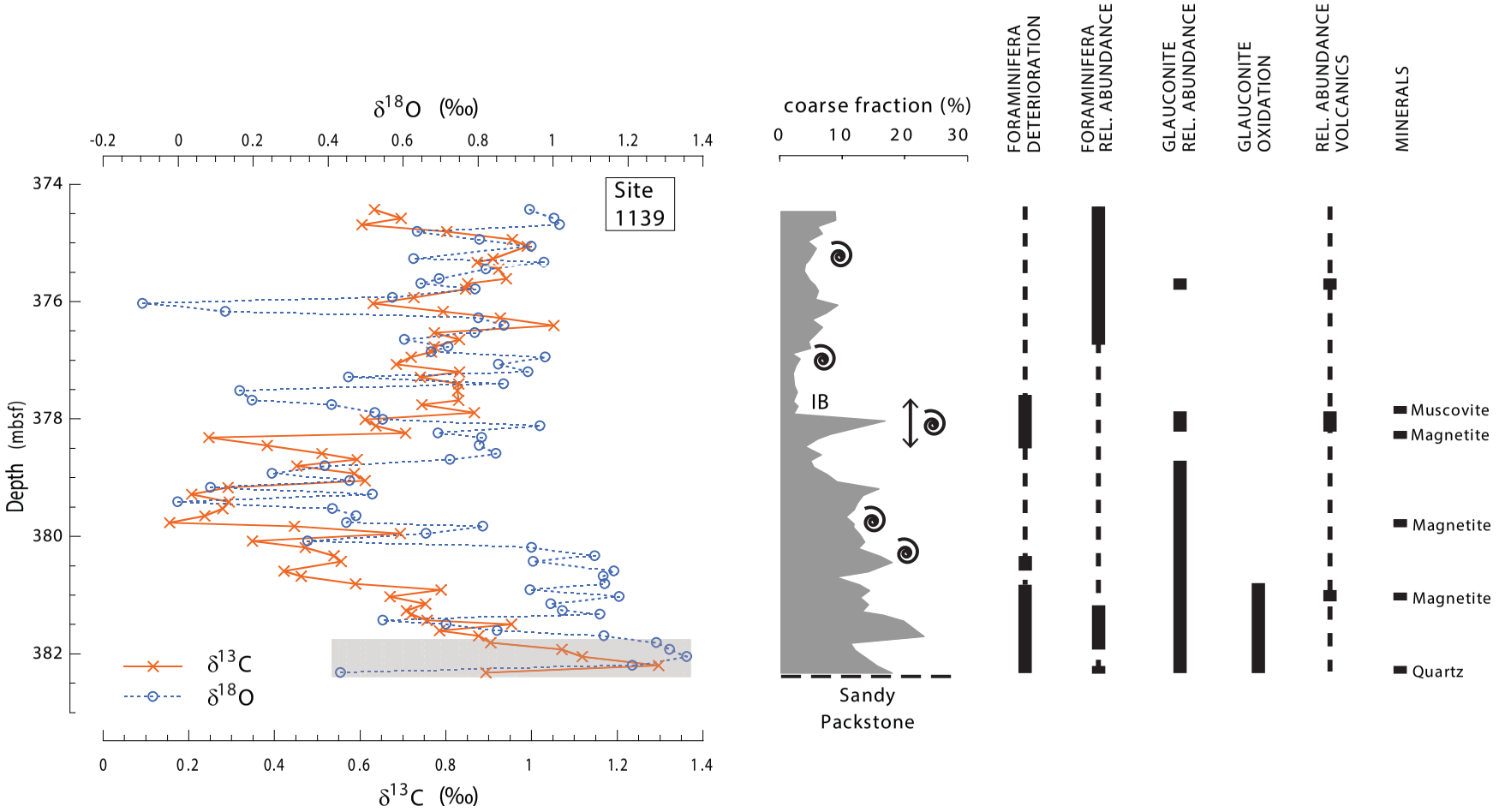

Figure 5.2: Site 1139 benthic foraminifera *C. mundulus* δ^{13}C and δ^{18}O records produced in this study plotted against depth and compared to coarse fraction weight %, foraminifera preservation and lithologic assessments. Grey shading tentatively indicates step-2 of the characteristic EOT (Figure 2.1). Coarse fraction weight % and lithological features are represented to the right. (Spirals: occurrence of unusually large benthic foraminifera specimens ($> 500\mu m$), IB: infaunal benthic (i.e. *Uvigerina* spp. and unilocular forms).

5.3.3 Site 1140

Weight % coarse fraction as well as qualitative assessments of foraminifera preservation, foraminifera relative abundance and dolomitization of the foraminifera tests are shown in Figure 5.3.

The new Site 1140 δ^{18}O and δ^{13}C records have the clearest signal of the E-O isotopic step as recorded globally, and the strongest correlation between δ^{18}O and δ^{13}C among the Leg 183 sites studied here.

The lowermost five δ^{18}O values (234.5 - 234.2 mbsf) trending towards higher values by 1.35 to 1.75 ‰ were offset from the δ^{13}C. Sitting directly above igneous basement at this site, these values could represent diagenetically altered outliers with an isotopic enrichment caused by partial dolomitization of the original calcite tests as suggested by large secondary crystals in SEM view (Plate 3). Despite the offset in these few values, visual inspection suggests that both curves show increase in isotopic values of $\sim$ 1.10‰ δ^{18}O, and $\sim$ 0.8‰ δ^{13}C from $\sim$ 233.5 - 231.5 mbsf (see shaded area in Figure 5.3), that I interpret as corresponding to the global isotopic increase characteristic of the EOT (Zachos et al., 1999; Coxall and Pearson, 2007; Coxall and Wilson, 2011). A distinct maxima in both isotope curves is reached between 232 - 231.5 mbsf. As in Site 1139, after the isotopic peak, δ^{18}O values remain high while the δ^{13}C recovers between 231 - 230 mbsf. Thereafter both isotopic values shows a plateau of 1.35 ‰ in δ^{13}C and of 1.5 ‰ in δ^{18}O until an abrupt decrease of $\sim$ 0.4‰ in δ^{13}C at 228 mbsf restoring to its initial values in the deeper section.

In contrast to the other sites, Site 1140 appears to show a lag of δ^{18}O with respect of δ^{13}C immediately before the isotope peak at $\sim$ 232 mbsf, where there is a local decrease in δ^{18}O values.

Site 1140 sand fraction

Optical observation shows that diagenesis is affecting the microfossils at Site 1140. This is evidenced by deteriorating microfossil preservation by dolomitization (section 5.2.3, Plate 3). Down core 1140-25R there is higher presence of rhomobohedral crystals of dolomite overgrowing the calcite of the foraminifera test walls. Dolomite is an authigenic mineral that might have formed in the sediments post-buried as a result of the hydrothermal activity present near this site during the early Oligocene (Coffin et al., 2000). The deepest studied sample (183-1140A-25R-CC) is almost barren of foraminifera tests since the shells appear extensively recrystallized to sand-sized rhombohedral crystals of dolomite that dominate the 63 - 150 μm size fraction. Thus, six benthic foraminifera samples from the last section (1140A-25R-5) were run in the mass spectrometer with just the half mass (0.1 mg) of the standard (0.2 mg).

An increase in infaunal benthic species in the $> 250\mu m$ size fraction occurs in intervals: 1140A-25R-4, 7 - 9 cm (232.17 mbsf), 1140A-25R-3, 142 - 144 cm (232.02 mbsf) and 1140A-25R-3, 129.5 - 131.5 cm (231.895 mbsf).

Weight % coarse fraction. The samples from this site 1140 had the lowest values of weight % coarse fraction ($\sim$ 3 - 16 %) of the three Leg 183 sites studied here consistent with its lithology (nannofossil chalk). The maximum proportion of weight % coarse fraction, 16%, is found down-section core 1140-25R (sample 1140A-25R-5, 10 - 12 cm, 233.7 mbsf).

This baseline increase in coarse fraction could be related to the large dolomitization of the biogenic material. The isotope peak at $\sim$ 232 mbsf is followed by a slight increase of $\sim$ 5 % in the amount of coarse fraction.

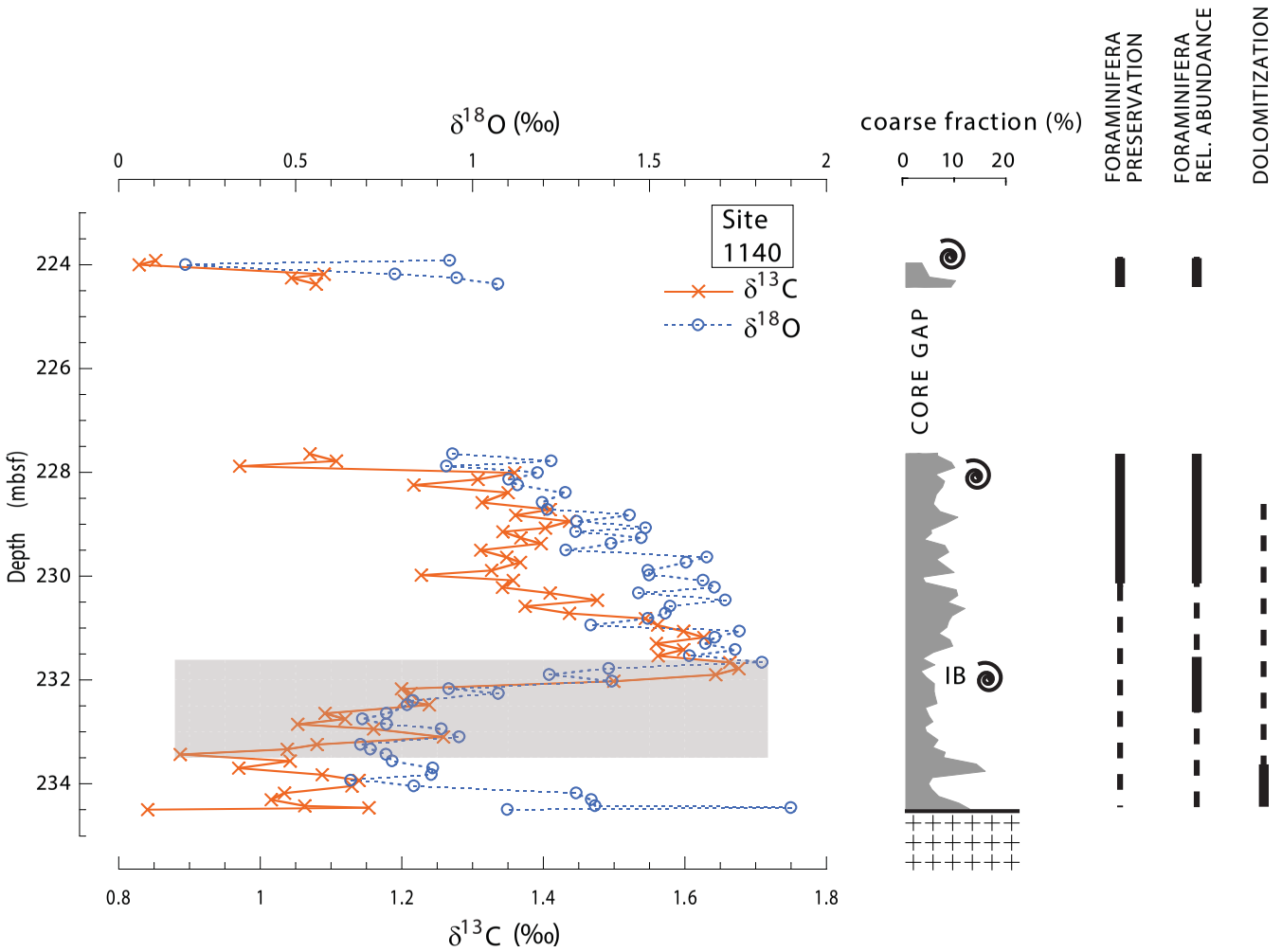

Figure 5.3: Site 1140 benthic foraminifera *C. mundulus* δ^{13}C and δ^{18}O records produced in this study plotted against depth and compared to coarse fraction weight %, foraminifera preservation and lithologic assessments. The shaded area identifies a $\sim$ 1.10‰ increase in δ^{18}O and $\sim$ 0.8‰ increase in δ^{13}C from $\sim$ 233.5 - 231.5 mbsf that I interpret as corresponding to the global isotopic increase characteristic of the EOT (Figure 2.1). Coarse fraction weight % and lithological features are represented to the right. (Spirals: occurrence of unusually large benthic foraminifera specimens ($> 500\mu m$), IB: infaunal benthic (i.e. *Uvigerina* spp. and unilocular forms).

5.4 Chemostratigraphic correlation across the Kerguelen Plateau

The Site 1138, 1139 and 1140 isotope records were compared to a published benthic foraminifera (*Cibicidoides* spp.) stable isotope record from ODP Site 744 (Zachos et al., 1996). The Site 744 record aided chemostratigraphic correlation for several reasons: (i) it presents continuous coverage of the EOT interval from undisturbed sediment records from SKP; (ii) it is located at 2307.3 m, then is bathed by intermediate waters, as are the new study sites; (iii) the carbon and oxygen isotope records were recovered on same benthic foraminifera genus, *Cibicidoides* spp., permitting direct comparison of values; (iv) the site shows low sedimentation rates of ($\sim$ 10 m/Myr) comparable to those of the new sites (Appendix A, Figures A.1, A.2, A.3); and (v) all sites had similar sampling spacings ($\sim$ 10 cm) allowing for a similar temporal resolution of the samples. Furthermore, since the chemostratigraphic signal happened globally and synchronous, the fit served as an additional dating tool that helped to improve the age-model. The age-model at these high latitude sites is weak since there is a lack of strong biostratigraphic markers.

In order to do this correlation, the Leg 183 core depths were converted to ages (in millions of years) using the biostratigraphic data available from the Shipboard Scientific Party (Coffin et al., 2000). To test and refine the biostratigraphic framework I also integrated existing paleomagnetic data for the sites. The shipboard paleomagnetic inclination data (Coffin et al., 2000) from Sites 1138 and 1139 across the studied interval is highly variable, hindering its interpretation. In contrast, Site 1140 presented well constrained paleomagnetic data for magnetic reversal C13r (Figure 5.4), which is useful for constraining the late Eocene to basal Oligocene. All sites use the same chronologic framework (Cande and Kent, 1995). I emphasize that there are likely large uncertainties in the 1138, 1139 and 1140 age models. This leads to site-to-site mismatches in age when trying to align the isotope features. Nonetheless, the correlation with Site 744 reveals how much of the characteristic EOT is present from the new stable isotope records aiding to constrain the age. The chemostratigraphic correlation of the four sites is shown in Figure 5.4 and the patterns observed were:

5.4.1 Site 744

The reference Site 744 shows the general EOT pattern of $\sim$ 1 ‰ increase in δ^{13}C and $\sim$ 1.5 ‰ increase δ^{18}O in the latest Eocene - early Oligocene (Figure 5.4). The peak values in both isotopes are reached in the basal Oligocene associated with normal magnetic chron C13n. The δ^{18}O shows a baseline shift whilst δ^{13}C excursion recovered to values close to late Eocene baseline.

5.4.2 Site 1138

Planktonic foraminifera

Shipboard biostatigraphic studies show an early Oligocene age (Zone AP13) across the studied intervals (Figure 5.4). The planktonic foraminifera biostratigraphic ages for the

core investigated (1138-36R) are defined by the absence of late Eocene *G. index* and the presence of *Subbotina angiporoides* (Coffin et al., 2000).

Calcareous nannofossils

The oldest data plotted in Figure 5.4 (sample 183-1138A-36R-CC) contains *Reticulofenestra umbilica*, *Isthmolithus recurvus* and *Reticulofenestra oamaruensis*. This biostratigraphic assemblage belongs to the *R. oamaruensis* Zone, which straddles the Oligocene/Eocene boundary (Coffin et al., 2000).

Chemostratigraphic correlation

Based on comparison with Site 744 and biostratigraphic descriptions, Site 1138 appears to contain Oi-1. The Site 1138 isotope increase within magnetic Chron C13n is of $\sim 1‰$ in $\delta^{13}C$ and $\sim 1.2‰$ in $\delta^{18}O$ that is thought to represent Oi-1. Assuming linear sedimentation rates, the entire Site 1138 isotopic sequence spans ~ 600 ka. In comparison to Figure 2.1, the entire sequence might represent the top limit of 'step 1', the 200 ka plateau, 'step 2' (Oi-1) and the 400 ka of maxima values.

5.4.3 Site 1139

Planktonic foraminifera

The oldest sample analyzed (183-1139-40R-CC, 383.5 mbsf) had a maximum age from 34.3 30.3 Ma. This is estimated by the occurrence of *Subbotina angiporoides* in the absence of late Eocene *G. index* (Coffin et al., 2000).

Calcareous nannofossil

The oldest data point represented in 5.4 (sample 183-1139A-40R-CC) lies within nannofossil Zones *Blackites spinosa* to *R. oamaruensis*. It spans a wide range of ages after the co-ocurrence of *Blackites spinosa*, *I. recurvus*, *Coccolithus formosus* and *Clausicoccus fenestratus*. *Blackites spinosa* abounds in Sample 183-1139A-40R-5, 25-27 cm; 380 mbsf (data point at 33.3 Ma) (Coffin et al., 2000). The sample does not present *Discoaster saipanensis* or *R. oamaruensis* (Wei, 1992).

Chemostratigraphic correlation

The isotope curves for Site 1139 were challenging to correlate with Site 744. Based on the biostratigraphic descriptions the peaks in $\delta^{13}C$ and $\delta^{18}O$ at the base of the record correlate to maxima Oi-1 values. The presented enrichment is of 1.0 ‰ in $\delta^{18}O$ and 0.4 ‰ in $\delta^{13}C$. Both isotope values are $> 1‰$ lighter than Site 744, but these follow the cyclicity of Site 744 chemostratigraphy. The new record spans 700 ka assuming constant sedimentation rates. In comparison to the entire EOT shown in Figure 2.1, this new record covers the top limit of 'step 2' and Oi-1.

5.4.4 Site 1140

The site contains paleomagnetic data correlated with biostratigraphic data. This creates the strongest age model of the three sites.

Planktonic foraminifera

The early Oligocene was established by the presence of *S. angiporoides* (Zone AP13) in sample 183-1140A-25R-4, 135-139 cm; $\sim$ 233.4 mbsf (Coffin et al., 2000), represented by the data point at 33.73 Ma in Figure 5.4.

Calcareous nannofossil

The core catcher sample from core 183-1140A-24R, at $\sim$ 224 mbsf (fourth and fifth youngest data points in Figure 5.4) belongs to the *Reticulofenestra daviesii* Zone, but is problematic sample since it covers a wide biostratigraphic age range from the late Oligocene to the early Oligocene. It contains *R. umbilica*, *C. fenestratus*, *Blackites spinosus*, two specimens of *Coccolithus formosus*, and a single specimen of *Isthmolithus recurvus* (the latter two thought to be reworked) (Coffin et al., 2000). Downcore, the second oldest data point in Figure 5.4 (sample 183-1140A-25R-5, 90 cm ; 234.48 mbsf) holds *Isthmolithus recurvus*, *R. umbilicus* and *C. formosus*. The last data point (core catcher sample 183-1140A-25R-CC; 234.5 mbsf), shows a broad biostratigraphic range from nannofossil Zones CP16a/b to CP15b (Coffin et al., 2000).

Paleomagnetism

This age model suggests that the normal-reversed sequence at $\sim$ 230 mbsf (below interval 183-1140A-25R-4, 0-30 cm) may correlate with magnetic boundaries Chrons C12n/r or C13n/r (33.5 Ma). This latest was the age used in the age model of this Site.

Chemostratigraphic correlation

A strong, clear correlation of both δ^{13}C and δ^{18}O dynamics and calculated ages, can be drawn between Sites 1140 and 744. The use of the age-depth for C13r/C13n at Site 1140 matches with Site 744 chemostratigraphy. It has only been applied a $\sim 50ka$ age readjustment shown as a temporal sub-axis in Figure 5.4, since both chemostratigraphic profiles showed a better match. The five youngest data plotted are thought to belong biostratigraphically to the *Reticulofenestra daviesii* Zone. Here, the linear sedimentation rates need to have increased to be within this zone.

The site depicts the most clear chemostratigraphic pattern of the EOT compared to Figure 2.1. This is shown by the presence of the entire eccentricity cycle of 400 ka cyclicity that characterizes Oi-1 within roughly the duration of magnetochron C13n.

In terms of absolute isotopic values, the δ^{18}O values are $\sim$ 0.5 - 0.75 ‰ lower than Site 744, whereas $\delta^{13}C$ values are very similar to Site 744 5.4. The isotope increase is of $\sim$ 1.10‰ increase in δ^{18}O and $\sim$ 0.8‰ in δ^{13}C and the former lags by c. 20 ka the latter at Oi-1.

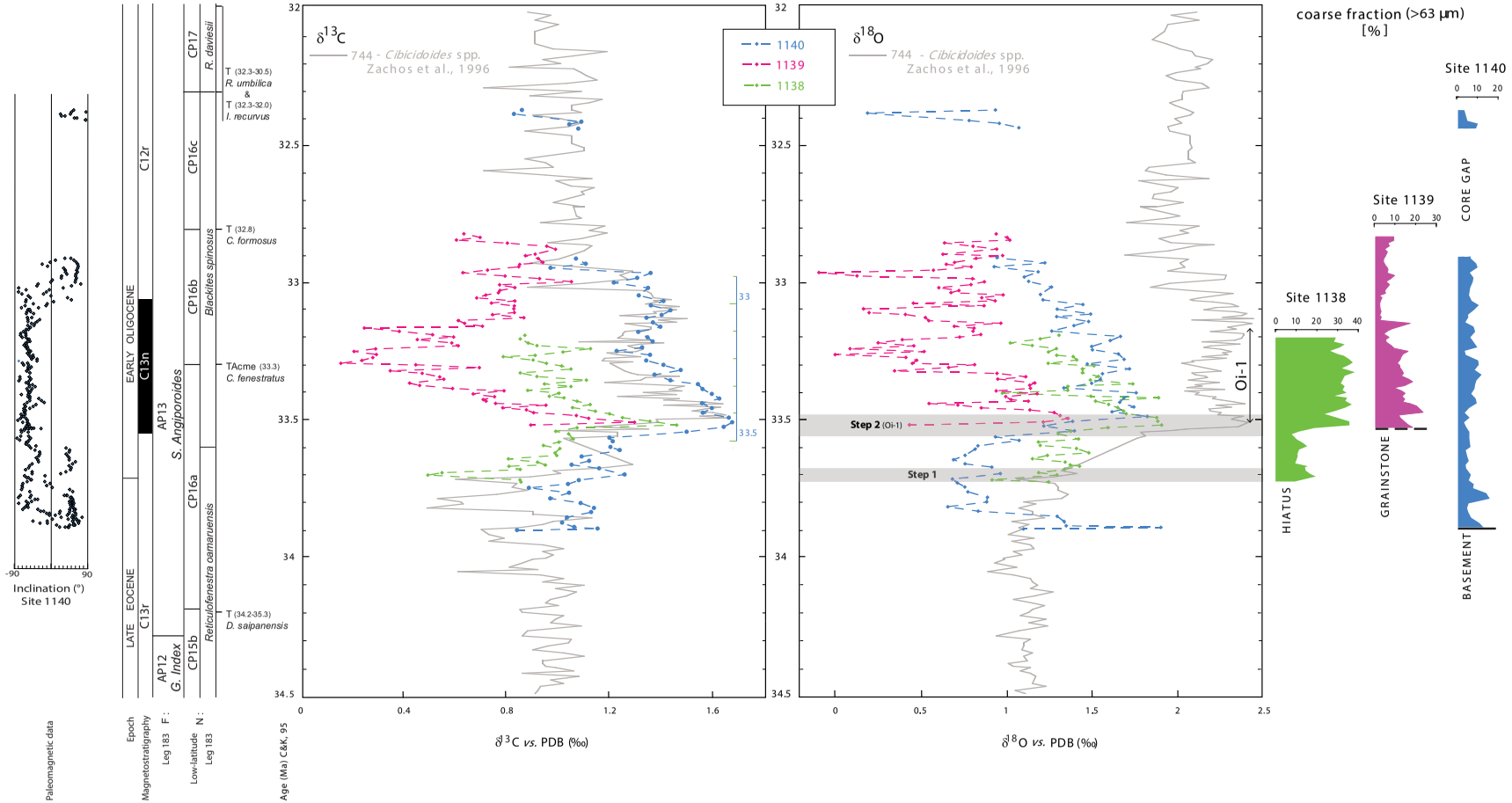

Figure 5.4: Benthic foraminifera (*Cibicidoides* spp.) isotope data from Sites 1138, 1139 and 1140 plotted against depth after age-model and chemostratigraphic correlations with Site 744. Numerical ages are those of Cande and Kent (1995). F: planktonic foraminifera datum events; N: calcareous nannofossil, T: top and B: bottom datum events of calcareous nannofossil occurrence.

5.5 E-O chemostratigraphic compilation.

The new isotope results from Sites 1138, 1139, and 1140 were compared with previously published benthic stable isotope records for the time interval between 34.5 and 32 Ma to place the new data in a global context. The comparison includes three more sites from the KP (ODP Site 748 (Zachos et al., 1992; 1994), ODP Leg 119 Sites 744 (Zachos et al., 1996) and 738 (Barrera and Huber, 1991)), two from the Atlantic sector of the Southern Ocean (ODP Sites 689 (Diester-Haass and Zahn, 1996), and 690 (Kennett and Stott, 1990)) and one site from the equatorial Pacific (ODP Site 1218, (Coxall et al., 2005)). Their location is shown in Table 5.1 and Figure 5.5.

The goal of this was to optimize the KP latitudinal transect, and obtain a more holistic view of deep ocean changes across the EOT both within and outside the Southern Ocean. The use of the Site 1218 record from the eastern equatorial Pacific is significant since it represents the highest resolution orbitally-tuned sequence across the EOT (Coxall et al., 2005). Note from Table 5.1 that all sites except Site 1218 are located at intermediate water depths, and would therefore be bathed in 'intermediate water masses' at the sea floor, whereas Site 1218 would be expected to record true 'bottom' water flow.

Site	location	water depth (m)	paleodepth (m)	source
1218	Equatorial Pacific	4826	3900	Coxall and Wilson (2011)
1140	NKP	2394	2000	this study
1139	NKP	1415	1000	this study
1138	CKP	1141	1000	this study
748	SKP	1288	1200	Zachos et al. (1992; 1994)
744	SKP	2307	2300	Zachos et al. (1996)
738	SKP	2263	2000	Barrera and Huber (1991)
689	Maud Rise	2080	1700	Diester-Haass and Zahn (1996)
690	Maud Rise	2914	2500	Kennett and Stott (1990)

Table 5.1: All sites and their modern and E/O water depths integrated into the global comparison.

Overall, the benthic foraminifera chemostratigraphic synthesis shown in Figure 5.6 depicts stronger correlation in δ^{13}C between KP and other widely distributed EOT sequences than in δ^{18}O. The exception is Site 1138 and 1139 δ^{13}C which record lower δ^{13}C by $\sim$ 0.3 ‰ than the other sites. Starting with the δ^{13}C (Figure 5.6, plot A), the Eocene part of the isotope record shows the highest amplitude variability ($\sim$ 0.9‰) within sites, but the absolute values are relatively similar (+/- $\sim$ 0.3‰) in the late Eocene. The records from equatorial Pacific show the lightest values and the ones in Maud Rise the heaviest. From step-1 of EOT there are very similar absolute values and systematic changes in Sites 1218, 1140, 748, 744 and 689. After reaching the Oi-1 peak, δ^{13}C values continued high, following a 400 ka cyclicity band until reaching $\sim$ 33 Ma where they began decreasing gradually and started to show slight variations up to $\sim$ 0.6‰ between the sites. The values differ again from lighter in the Equatorial Pacific to heavier in the KP. The new Site 1140 record from the northern tip of KP, mirrors interestingly the high resolution benthic δ^{13}C trend from Site 1218, and it is also a close match to Sites 744, 748, 689 and 690. Sites 1138 benthic δ^{13}C was similar to other KP sites and Sites 689 and 1218 in the late Eocene and at the Oi-1 peak, but it diverged significantly during the early Oligocene together with Site 1139.

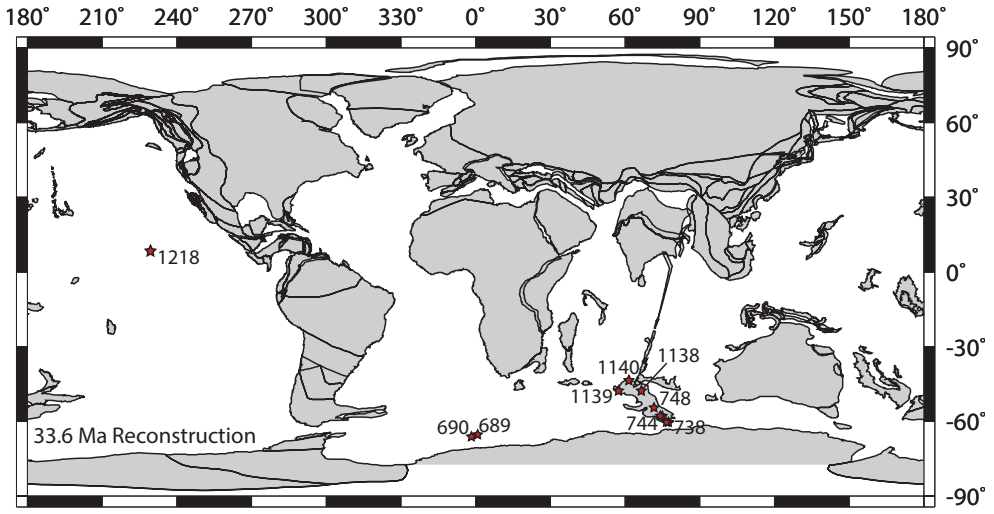

Figure 5.5: Early Oligocene paleogeographic reconstruction of all sites presented in the chemostratigraphic synthesis of this study. Base map elaborated by Ocean Drilling Stratigraphic Network (ODSN, 2013).

Focusing on the δ^{18}O profiles (Figure 5.6, plot B), Sites 1218, 1140, 1138, 748, 744 and 689 had similar values in the late Eocene until reaching step-1. After step-1, big δ^{18}O changes are introduced, Site 1218 , 1140 and 1138 separate from the rest. From step-2 into Oi-1 there is a big diversification of ocean temperature layers. The multi-site comparison suggests that δ^{18}O latitudinal gradients markedly increase in variablity after the Oi-1 peak, from $\sim$ 0.5‰ in the late Eocene to $\sim$ 1‰ in the early Oligocene. The high-latitude sites (Sites 690, 689) and SKP sites (Sites 738, 744 and 748) show higher δ^{18}O values than the low latitude Site 1218 and the three new sites at NKP throughout the covered 34.5 and 32 Ma. This characteristic east-west longitudinal gradient suggests that the deep ocean at that Site 1218 and new NKP sites had lower benthic δ^{18}O compared to the SKP and Weddell Sea. If we assume that lower δ^{18}O represents relatively warmer bottom water temperatures, then this result suggests that the subsurface water mass over NKP was more similar to that in the equatorial Pacific than to the high southern latitudes at sites from SKP (Sites 748, 744, 738) and Weddell Sea (689, 690). Specifically, the modern water depth of both Site 1140 (NKP) and 744 (SKP) is almost the same ($\sim$ 2350 m). Interestingly, in the late Eocene, δ^{18}O values were lighter by $\sim$ 0.4 ‰, but after Oi-1 this difference increased gradually by $\sim$ 1‰ during the early Oligocene, suggesting different ocean temperature conditions between the intermediate waters from northern and southern KP. After the global Oi-1 event in the early Oligocene, δ^{18}O values from Equatorial Pacific and NKP decreased by about $\sim$ 0.5‰, while values from Weddell Sea and SKP (the closest to Antarctica) remained close to 2‰. This δ^{18}O difference between sites at these locations persisted during the Oligocene. A final observation is that for all sites composed within the represented early Oligocene, the carbon isotopes values return to those found in the late Eocene, whilst the oxygen isotopes remain high, although lower than Oi-1 peaks. This is consistent with the view that δ^{18}O signal includes a baseline shift in the δ^{18}O of sea water due to storage of ^{16}O in semi-permanent Antarctic glaciation, where as the δ^{13}C change represents a temporary carbon-system response to the ocean-climate change.

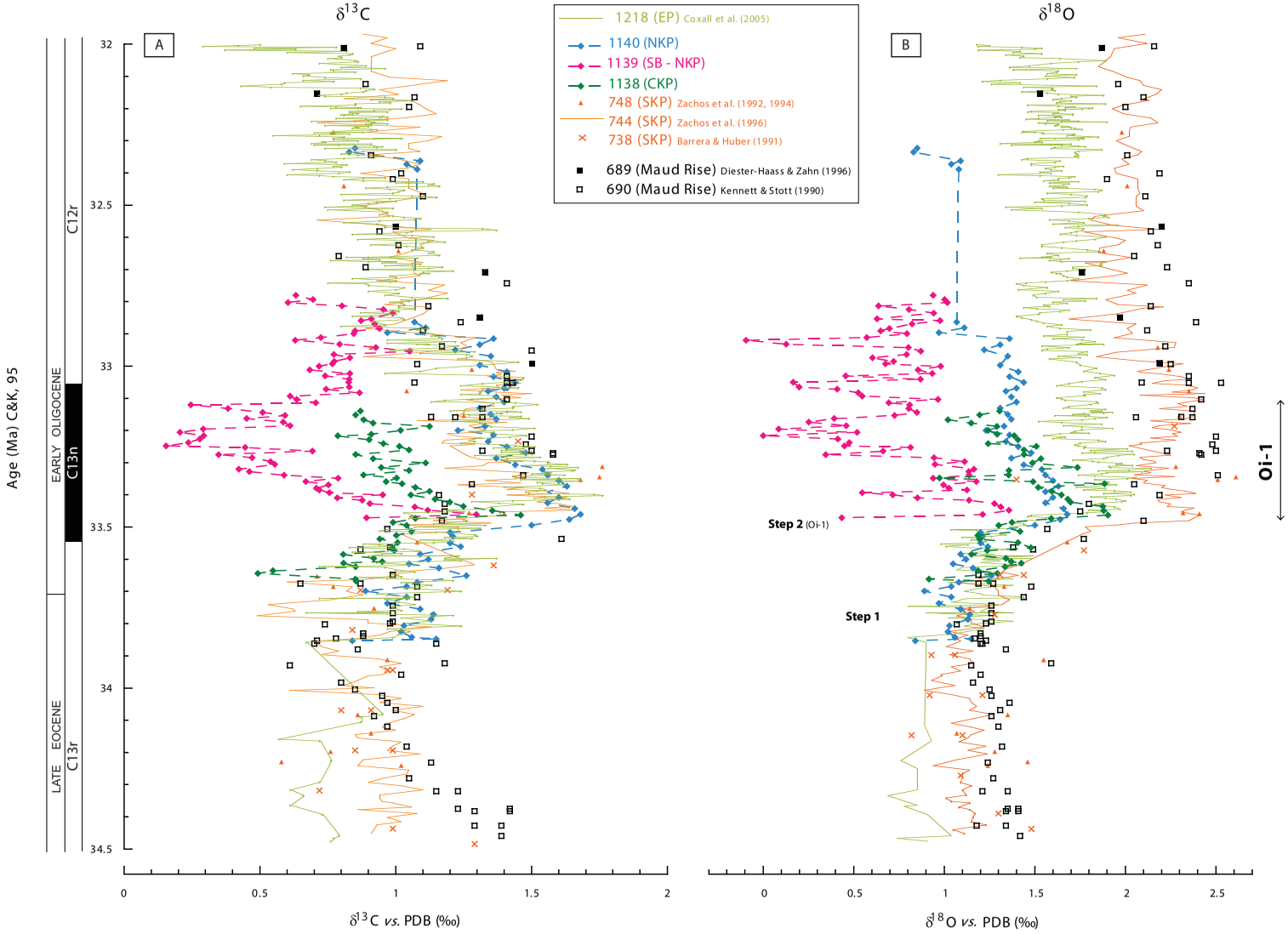

Figure 5.6: Early Oligocene / Late Eocene benthic foraminifera stable isotopes comparisons between all available sites on the KP, sites from the Southern Ocean sector of the Atlantic (Maud Rise) and equatorial Pacific. Ages according to Cande and Kent (1995).

Chapter 6

Discussion

The first part of the discussion focusses on integrating limitations, observations and inferences of the sediment samples and their isotope results. A more broad interpretation follows, provided by a synthesis of all KP benthic stable isotope records, and then globally to help interpreting the dynamics of oceanographic changes across the latitudes of the KP.

6.1 Lithological characteristics

A primary limitation is given by the rotary coring from which the samples were retrieved. This technique creates core disturbances in the soft sediment as drilling slurry and 'biscuits' (Appendix A, Figure A.2) and discontinuous core recovery. However, the isotope analysis indicate EOT coherent stratigraphy that permits large scale paleoceanographic interpretations.

Differences in the relative proportion of coarse and fine fractions as well as sediment lithology can be meaningful in assessing past changes in surface ocean processes including e.g. primary productivity, carbonate preservation (Rothwell, 1989). I emphasize that % weight coarse fraction is a relative estimate since it is influenced by more than one process (Salamy and Zachos, 1999). Sites 1138 is located at 1141 m water depth and represents the shallowest site on the central part of the northern KP. Carbonate dissolution is more substancial in this site judging from the dissolution holes and chamber damage in the planktonic and benthic foraminifera tests. Due to the shallow bathymetry of the site, the sequence should be above the EOT lysocline. The carbonate dissolution, therefore, is attributed to a rise in the supply of organic carbon to the sea-floor that promotes calcite dissolution during its oxidation (which lowers pore-water pH) (Diester-Haass, 1995). Another feature that indicates E/O boundary related surface ocean changes at this site comes from the glauconitic content within the sections from Sites 1138 and 1139. The shift into diagenetic glauconite precipitation is associated to water masses with higher organic matter content, consistent with the lower values in δ^{13}C at Sites 1138 and 1139. Moreover, some intervals at the three sites presented unusually large benthic and infaunal benthic foraminifera. This can be linked to the isotopic shift product of higher productivity driven by enhanced mixing of the ocean (Salamy and Zachos, 1999; Diester-Haass and Zachos, 2003). The presence of igneous basement underlying the studied samples in Site 1140 would have promoted the recrystallization of dolomite at the lowermost sedimentary core 183-1140-25R (Plate 3).

6.1.1 Insights into paleoproductivity

ODP sites from SKP (Sites 738, 744 and 748; Figure 3.2) show an increase in biogenic silica production and deposition at the EOT. However, climatic cooling at the E/O boundary is not associated with the onset of biosiliceous facies at any of the three sites studied here from the NKP and CKP. This suggests that the silica productivity change affected only the southern part of the KP. Therefore, assuming that an Antarctic Polar Front associated with a biofacies change product of colder waters developed at the EOT, it should have been located south of the central region of CKP ($\sim 58°$S). This cold nutrient-rich waters bathing SKP could also be derived from sinking of polar cold-waters sourced close to a greatly cooled Antarctica glaciated margin and not as a response to the front itself (Barker and Thomas, 2004).

On the other hand, although there is no biosilica, the studied EOT sequence at Sites 1138, 1139 and 1140 represent an increase in coarse fraction at Oi-1 event (Figure 5.4). Specifically, Sites 1138 and 1139 present at Oi-1 event higher planktonic foraminifera abundance and unusually large benthic foraminifera combined with increased glauconite and dissolution, all of which provide an indication of enhanced primary productivity.

6.2 Southern Indian Ocean circulation changes at the EOT

The new benthic foraminifera stable isotope data set from Site 1140 complies with the global chemostratigraphic signal of the EOT showing an abrupt increase in δ^{18}O and δ^{13}C, indicating that there is a relatively complete copy of the sequence presented above basement at this Site. This notion is supported by the dynamics in Site 1140 stable isotope records similar to that observed from the reference Site 744 (Zachos et al., 1996), more evident in the δ^{13}C signal. The amplitude of both isotopic shifts in Site 1140 recorded in Chron C13n follows the low-amplitude orbital forcing change in obliquity (400 ka) that paced Antarctic ice-sheet growth. Indeed, this correlation has helped to improve the age of the recovered material. This is significant because it gives a constraint on deep ocean changes on the NKP, expanding $\sim 13°$ latitude north of the existing SKP sites.

On the North-central and North-eastern KP the isotope results from Sites 1138 and 1139 respectively, show significant differences (lower values) locally over KP and globally. The presence of diagenetic glauconite filling and overgrowing the test of benthic specimens at Sites 1138 and 1139 (Plate 1 and Plate 2 respectively) indicate significant diagenetic alteration that could have produced some of the offset values between carbon and oxygen isotopes. Because of this, it was more challenging to correlate the sites. However, based on the biostratigraphic descriptions available from the Shipboard Scientific Party of Leg 183 (Coffin et al., 2000), there appears key portions of the latest Eocene, step-1 and step-2 at Site 1138; and the basal Oligocene starting from the bottom of Oi-1 in Sites 1138 and 1139 (Figure 5.4). These were the isotopic shifts that I have tentatively correlated with the reference record Site 744 (Zachos et al., 1996).

As seen from the vertical isotope gradients in the age domain (Figure 5.6), there are major offsets in the carbon and oxygen isotope records between sites on the KP and globally. Overall, the oxygen isotope values at the three new NKP sites are lighter and

more similar to the late Eocene values compared to SKP sites, Atlantic sector of the Southern Ocean and the Equatorial Pacific. There are various possibilities to explain these differences. First, it is noteworthy that the EOT samples from the Leg 183 are more deeply buried (Figure 3.2) than for instance SKP Site 744 (Site 744 is shallower $\sim$ 100 km than Site 1140, $\sim$ 200 km than 1138, and $\sim$ 250 m than 1139). Therefore, it is possible that these lighter values are the result of thermal diagenesis at depth which can lead to depleted values. However, a 1‰ enrichment in δ^{18}O is still obtained across the EOT at Sites 1138 and 1140, suggesting that the absolute δ^{18}O shifts characteristics of the EOT are preserved. The extremely high amplitude of short-term variability within δ^{18}O and δ^{13}C in Site 1139 may be consistent with a diagenetic overprint. These high variation values are not thought to be artefact of the mass spectrometer analysis run with half of the standard mass, since these come from both standard and reduced benthic sample weights. The lack of enough specimens of the same size-fractions at all intervals (Appendix B) could have originated this higher variability as a result of varying vital-effects between specimens. However this variability should be much lower than the present on accounts only of the vital effects.

Another source of uncertainty and explanation for some of the differences between δ^{18}O and δ^{13}C at Site 1139 is uncertainty in age models. I suggest that especially for Sites 1138 and 1139 I have less confidence in the chronology. This is because there are large biostratigraphic uncertainties with few and poorly constrained datum events, and noisy magnetostratigraphic profiles. Furthermore, it is important to note that the age model approximations are based upon a singular linear sedimentation rate spanning the entire EOT that does not account for possible increases in sedimentation rates that are likely if upwelling increased associated with EOT-strengthening of a polar front across the region.

6.2.1 Insights from benthic δ^{13}C KP latitudinal transect

The presented global correlation in Figure 5.6 plot A, shows the highest late Eocene values for δ^{13}C at 34.5 Ma from Site 689 at Maud Rise. This suggests the presence of a distinct intermediate water-mass bathing the Southern Ocean sector of the Atlantic. This regional water mass could be primarily sourced from the Antarctic margin throughout this time interval (Bohaty et al., 2012). At this time, SKP δ^{13}C values are variable and the Equatorial Pacific reveals the lowest, but they converge to similar values in step-1 and during the Oi-1, despite the differences in water depth and latitudinal position in the Maud Rise, KP, and Equatorial Pacific. The convergence of δ^{13}C may be due to global changes in the size of the oceanic carbon reservoir involving an increased sea-floor burial of organic carbon at the EOT (Salamy and Zachos, 1999).

During the earliest Oligocene Oi-1 glaciation event, lighter benthic δ^{13}C is shown at Sites 1138 and 1139 (between 1100-1500 m water depth respectively) with respect to the rest of the sites. Part of this light δ^{13}C signal could show a local increase in organic carbon accumulation (preferentially enriched in the light isotope of carbon, ^{12}C) without rapid burial. The high amounts of organic matter are supported by the presence of glauconite at both sites (Figures 5.1, 5.2). At 32 Ma the values return to pre-EOT δ^{13}C values at all sites examined, indicating that the carbon system change was temporary.

6.2.2 Insights from benthic δ^{18}O KP latitudinal transect

In general, all δ^{18}O site-to-site isotope comparisons (Figure 5.6, plot B) for the latest Eocene show similar values experiencing ice and same bottom water temperature. However, in the earliest Oligocene the three new records (Sites 1138, 1139 and 1149) from CKP and NKP differ by more than 1 ‰ the values of SKP. This represents paleoceanographic changes affecting central, north eastern and northernmost KP differentially during Oi-1 compared to SKP. Site 1140 and 744 δ^{13}C is almost identical in absolute terms, but the δ^{13}C from Site 1138 and 1139 are lower by several decimals ‰. Thus, the big early Oligocene offset in δ^{18}O between new Leg 183 sites and other sites at the KP might relate to latitudinal ocean temperature changes at these intermediate water depths.

The effects of changes in δ^{18}O due to ice volume changes are globally synchronous (Bohaty et al., 2012). The observed offsets in δ^{18} after the EOT in the three new sites could be interpreted as if the NKP was isolated from the SKP with a more stratified and warmer intermediate water mass. The fact that the northermost KP Site 1140 shows lighter values in δ^{18}O but not in δ^{13}C is consistent with a non diagenetically affected signal, thus suggesting that the presence of waters bathing the northern tip of KP were more influenced by warmer and saltier southern Indian Ocean waters product of a still open Tethys Sea. On the other hand, the SKP became dominated by ocean circulation associated with a 'proto-ACC' cross-cutting the KP. This idea is supported by the records from the Maud Rise and SKP that show high δ^{18}O evoking the presence of colder intermediate waters bathing the Weddell Sea (Sites 689 and 690) similar to those intermediate waters bathing SKP. The fact that they show similar dynamics and absolute values in δ^{18}O and δ^{13}C during the entire EOT suggests that there was no major change in the circulation pathway, at the time, although cooling of the common deep water mass was likely. Strengthening of the ACC during the late Oligocene may account for this.

On the other hand, the deep waters outside the Southern Ocean from lower-latitude Site 1218 despite being $\sim$ 2000 m deeper, show warmer temperatures. This was likely the product of a highly mixed bottom water-mass in the vast Pacific Ocean, possibly with north Pacific deep-water mixed in, that was different to the colder Antarctic sources.

The pattern of higher δ^{18}O at the E/O cooling values did not restore to late Eocene values. This demonstrates the sustainment of Southern Ocean glaciation after the EOT keeping the ocean enriched in the heavy isotope.

Chapter 7

Conclusions

This research has produced Eocene-Oligocene δ^{13}C and δ^{18}O benthic foraminifera records for three new sites at the KP, bringing the total to six EOT sequences with deep-sea benthic stable isotope datasets. The three new records expand the northern latitudinal transect of the KP allowing for the first time a complete paleoceanographic interpretation across 20° latitude in a key region of the Southern Ocean sensitive to ocean climate change. This allowed to test the hypothesis about the impact of Antarctica glaciation in the establishment of a polar front across KP latitudes at the earliest Oligocene, applying two groups of proxies: (i) generation of stable isotopes in benthic foraminifera at three sites and synthesis with existing paleorecords at the KP, Atlantic sector of the Southern Ocean and Equatorial Pacific; and (ii) observation of lithologic/biomineral facies of the three new sites and comparison with the data at the EOT from other KP sites.

The results from the new stable benthic isotope records show that:

- The new benthic foraminifera δ^{18}O and δ^{13}C records from Sites 1140, 1139 and 1138 show evidence of deep-water cooling and global carbon reconfiguration at the EOT consistent with evidence found previously on the KP, elsewhere in the Southern Ocean and globally. This is shown by an enrichment of the heavy isotopes of oxygen and carbon towards the boundary from magnetochrons C13n/r.

- Northernmost KP Site 1140 has the most complete and coherent Eocene/Oligocene boundary sequence of the three new sites, as shown by its chemostratigraphic profile in comparison with the global EOT isotopic signal. This has allowed to refine the age model at this site showing that δ^{18}O shift within 232.17 - 232.02 mbsf correlates with the normal-reversed geomagnetic polarity sequence C13r/C13n.

- Sites 1138 and 1139 reveal isotope gradients that are less consistent with the existing EOT records. Despite this, they have been tentatively correlated to the E/O boundary based on their biostratigraphy. They may reflect a combination of local conditions, and especially SIte 1139, effects of diagenesis overprinting the original signal.

- Major differences in δ^{18}O between NKP and SKP appear in the earliest Oligocene that represent paleoceanographic changes affecting central, north eastern and northernmost KP differentially during Oi-1 compared to SKP. Lighter values in NKP

indicate relative warmer intermediate water masses, whilst heavier values in SKP suggests the presence of a colder water mass.

- The shallower Sites 1138 and 1139 reveal lighter $\delta^{13}C$ ($\sim$ 0.5 - 1 ‰ lighter) after the EOT, which diverge from Site 1140, the SKP and global signals, suggesting the presence of similar organic carbon (^{12}C) rich water masses. related to local elevated primary production and sea-floor organic flux, and/or influence of diagenetic overprints at Site 1139 (north-west KP).

From the lithologic/biomineral facies observations:

- No significant amounts of biosilica were found in the new sites across the EOT, since they present only calcareous microfossil remains. Previous studies showed increased biosilica on SKP at least in the basal Oligocene (ODP Sites 738, 744, 749, 748 and 747). This suggests that the onset of biosiliceous sedimentation, attributed to enhanced primary productivity due to upwelling of colder nutrient-rich waters, did not establish on NKP at the EOT. Thus, the polar front that today cross-cuts NKP is thought to have been located at northern SKP. This conclusion is in accord with the lower oxygen isotope values obtained at NKP with respect to SKP.

- There is an increase in glauconite content and planktonic foraminifera abundance after the EOT in Sites 1138 and 1139 associated with high presence of organic matter. This fact is consistent with the low $\delta^{13}C$ found after EOT at both Sites.

- Ice-rafted debris found at Site 1138 in the early Oligocene provides the first evidence of glaciers extending to sea-level releasing icebergs that reached the latitudes of CKP (53°S). This may indicate glaciers on the middle KP islands or icebergs derived from Antarctica.

On these bases, the results suggest that there are latitudinal paleoceanographic differences between South and North KP sites in the earliest Oligocene compared to latest Eocene. Presumably, northernmost KP was more influenced by warmer and saltier southern Indian Ocean waters, whereas SKP became dominated by colder water sourced from Antarctica. Future research including other Sites at the KP (e.g. Site 1137) could help constraining the hypothesis that changes in the Earth tectonic and climate system at the EOT resulted in a change of the polar front across the latitudes of the KP.

ACKNOWLEDGEMENTS
This thesis would not have been possible without the ease and endless inspiration from Dr. Helen Coxall. I thank the Curators at the Kochi Core Center for supplying Ocean Drilling Program sediment samples used in this study. I also appreciate Laura Martinez, for running the stable isotope samples. My special thanks goes to my dear parents Rafa and Montse, sister Gemma, big Coli & little Iris, and soul friends Neus and Matin for their support and precious time.

Bibliography

Arrhenius, G. (1952). Sediment cores from the East Pacific. *Reports of the Swedish Deep-Sea Expedition 1947-1948*, 1–227.

Barker, P. and E. Thomas (2004). Origin, signature and palaeoclimatic influence of the Antarctic Circumpolar Current. *Earth-Science Reviews* (66), 143–162.

Barrera, E. and B. Huber (1991). Paleogene and early Neogene oceanography of the southern Indian Ocean: Leg 119 foraminifer stable isotope results. In J. Barron, B. Larsen, and et al. (Eds.), *Proc. ODP, Sci. Results*, Volume 119, College Station, TX (ODP), pp. 693–717.

Barron, J., B. Larsen, and S. S. Party (1989). *Leg 119, Kerguelen Plateau and Prydz Bay, Antarctica*, Volume 119. College Station, TX (ODP).

Berger, W. (1973). Deep-sea carbonates: Pleistocene dissolution cycles. *Journal of Foraminiferal Research 3*(4), 187–195.

Berggren, W. (1992). Paleogene planktonic foraminifer magnetobiostratigraphy of the southern kerguelen plateau (sites 747-749). In J. Wise, S.W., R. Schlich, and et al. (Eds.), *Proc. ODP, Sci. Results*, Volume 120, College Station, TX (Ocean Drilling Program), pp. 551–568.

Berggren, W., D. Kent, C. Swisher, and M.-P. Aubry (1995). A revised cenozoic geochronology and chronostratigraphy. In W. Berggren, D. Kent, M.-P. Aubry, and J. Hardenbol (Eds.), *Geochronology, time scales and global stratigraphic correlation*, Number 54, pp. 129–212. SEPM Special Publication.

Bohaty, S., J. Zachos, and M. Delaney (2012). Foraminiferal Mg/Ca evidence for Southern Ocean cooling across the Eocene-Oligocene transition. *Earth and Planetary Science Letters* (317-318), 251–261.

Brady, H., W. Parker, and T. Jones (1888). On some foraminifera from the Abrolhos Bank. *Transactions of The Zoological Society 12*, 211–239.

Cande, S. and D. Kent (1995). Revised calibration of the geomagnetic polarity time scale for the Late Cretaceous and Cenozoic. *Journal of Geophysic Research 100*, 6093–6095.

Carter, L., I. McCave, and M. Williams (2008). Circulation and water masses of the Southern Ocean: A review. In F. Florindo and M. Siegert (Eds.), *Antarctic climate evolution*, Number 8 in Developments in Earth and Environmental Sciences, Chapter 4, pp. 85–114. Elsevier, Amsterdam.

Cloud, P. (1955). Physical limits of glauconite formation. *Am. Assoc. Petroleum Geologists Bull. 39*(4), 484–492.

Coffin, M., F. Frey, P. J. Wallace, and S. S. Party (2000). *Kerguelen Plateau Broken Ridge, Sites 1135 1142*, Volume 183. College Station, TX (ODP).

Cohen, K., S. Finney, and P. Gibbard (2013, January). International chronostratigraphic chart. *International Commission on Stratigraphy*.

Coxall, H. and P. Pearson (2007). The Eocene-Oligocene transition. In M. Williams and et al (Eds.), *Deep time perspectives on climate change: marrying the signal from computer models and biological processes*, pp. 351–387.

Coxall, H. K. and P. Wilson (2011). Early oligocene glaciation and productivity in the eastern equatorial Pacific: Insights into global carbon cycling. *Paleoceanography 26*(2), PA2221.

Coxall, H. K., P. A. Wilson, H. Pälike, C. H. Lear, and J. Backman (2005). Rapid stepwise onset of Antarctic glaciation and deeper calcite compensation in the Pacific Ocean. *Nature 433*, 53–57.

DeConto, R., D. Pollard, P. Wilson, H. Pälike, C. H. Lear, and M. Pagani (2008). Thresholds for cenozoic bipolar glaciation. *Nature* (455), 652–656.

DeConto, R. M. and D. Pollard (2003). Rapid Cenozoic glaciation of Antarctica induced by declining atmospheric CO_2. *Nature 421*(6920), 245–249.

Diester-Haass, L. (1995). Middle Eocene to early Oligocene paleoceanography of the Antarctic Ocean (Maud Rise, ODP Leg 13, Site 689): change from a low to a high productivity ocean. *Paleoceanography, Paleoclimatology and Paleoecology* (113), 311–334.

Diester-Haass, L. (1996). Late Eocene-Oligocene paleoceanography in the southern Indian Ocean (ODP: Site 744). *Paleogeography, Pleoclimatology, Paleoecology 130*, 99–119.

Diester-Haass, L. and J. Zachos (2003). The Eocene-Oligocene transition in the Equatorial Atlantic (ODP Site 925); paleoproductivity increase and positive d13C excursion. In D. Prothero, L. Ivany, and E. Nesbitt (Eds.), *From greenhouse to icehouse; the marine Eocene-Oligocene transition*, pp. 397–418. Columbia University Press. New York (USA).

Diester-Haass, L. and R. Zahn (1996). Eocene-Oligocene transition in the Southern Ocean: History of water mass circulation and biological productivity. *Geology 24*(2), 163–166.

Duncan, R. (1991). Age distribution of volcanism along aseismic ridges in the eastern Indian Ocean. In J. Weissel, J. Peirce, E. Taylor, and J. Alt (Eds.), *Proc. ODP, Sci. Results*, Volume 121, pp. 507–517.

Eagles, G., R. Livermore, and P. Morris (2006). Small basins in the Scotia Sea: The Eocene Drake Passage gateway. *Earth and Planetary Science Letters* (242), 343–353.

Ehrmann, W. and A. Mackensen (1992). Sedimentological evidence for the formation of an East Antarctic ice sheet in Eocene/Oligocene time. *Palaeogeography, Palaeoclimatology, Palaeoecology* (93), 85–112.

Emiliani, C. (1954). Depth habitats of some species of pelagic foraminifera as indicated by oxygen isotope ratios. *American Journal of Science* (252), 149–158.

Emiliani, C. (1955). Pleistocene temperatures. *Journal of Geology* (63), 538–578.

Epstein, S., R. Buchsbaum, H. Lowenstam, and H. Urey (1953). Revised carbonate-water isotopic temperature scale. *Geological Society of America Bulletin* (64), 1315–1325.

Gille, S. (1994). Mean sea surface height of the antarctic circumpolar current from geosat data: Method and application. *Journal of Geophysical Research 99*, 18255–18273.

Goodell, H. (1973). *Marine sediments of the Southern Oceans*, Volume 17 of *Antarct. Map Folio Ser.*, Chapter The sediments, pp. 1–12. New York: American Geographical Society,.

Graham, D., B. H. Corliss, M. L. Bender, and L. D. Keigwin (1981). Carbon and oxygen isotopic disequilibria of recent deep-sea benthic foraminifera. *Marine Micropaleontology* (6), 483–497.

Huber, B. (1991). Paleogene and early Neogene planktonic foraminifer biostratigraphy of ODP Leg 119 Sites 738 and 744, Kerguelen Plateau (southern Indian Ocean). In J. Barron, B. Larsen, and et al. (Eds.), *Proc. ODP, Sci. Results*, Volume 119, pp. 427–449. College Station, TX (ODP).

Jorissen, F., H. De Stigter, and J. Widmark (1995). A conceptual model explaining benthic foraminiferal microhabitats. *Marine Micropaleontology* (22), 3–15.

Kemp, E., L. Frakes, and D. Hayes (1975). Paleoclimatic significance of diachronous biogenic facies. In *DSDP, Init. Rep.*, Volume 28, pp. 909–918.

Kennett, J. (1977). Cenozoic evolution of Antarctic glaciation, the circum-Antarctic Ocean, and their impact on global paleoceanography. *Journal of geophysical reasearch 82*(27), 3843–3860.

Kennett, J. and N. Shackleton (1976). Oxygen isotopic evidence for the development of the psychrosphere 38 Myr ago. *Nature* (5551), 513–515.

Kennett, J. P. and L. D. Stott (1990). Proteus and Proto-Oceanus: ancestral Paleogene oceans as revealed from Antarctic stable isotopic results; ODP Leg 113. In P. Barker, J. Kennett, and et al. (Eds.), *Proceedings of the Ocean Drilling Program, Scientific Results* (College Station, TX (ODP) ed.), Volume 113, pp. 865–878. .

Lazarus, D. and J.-P. Caulet (1993). Cenozoic Southern Ocean reconstructions from sedimentologic, radiolarian and other microfossil data. In J. Kennett and D. Warnke (Eds.), *The Antarctic Paleoenvironment: A Perspective on Global Change. Part II.*, Number 60 in AGU Ant. Res. Ser., pp. 145–174.

Lear, C., T. Bailey, P. Pearson, H. Coxall, and Y. Rosenthal (2008). Cooling and ice growth across the Eocene-Oligocene transition. *Geology 36*, 251–254.

McCorkle, D. C., L. D. Keigwin, B. H. Corliss, and S. R. Emerson (1990). The influence of microhabitats on the carbon isotopic composition of deep-sea benthic foraminifera. *Paleoceanography 5*(2), 161–185.

Miller, K., R. Fairbanks, and M. G.S. (1987). Tertiary oxygen isotope synthesis, sea level history, and continental margin erosion. *Paleoceanography 2*(1), 1–19.

Miller, K. G., J. D. Wright, and R. G. Fairbanks (1991). Unlocking the Ice House: Oligocene-Miocene oxygen isotopes, eustasy, and margin erosion. *Journal of Geophysical Research: Solid Earth 96*(B4), 6829–6848.

Moore, J., M. Abbott, and J. Richman (1999). Location and dynamics of the Antarctic Polar Front from satellite sea surface temperature data. *J. Geophys. Res.* (104), 3059–3073.

Morgan, W. J. (1981). *Hotspot tracks and the opening of the Atlantic and Indian Oceans*, Volume 7: The Oceanic Lithosphere, pp. 443–487. New York: WileyInterscience.

ODSN (2013). Ocean drilling stratigraphic network: www.odsn.de (17-10-2013).

Orsi, A. H., I. T. Whitworth, and W. D. Nowlin (1995). On the meridional extent and fronts of the Antarctic Circumpolar Current. *Deep-Sea Research I 42*(5), 641–673.

Pagani, M., M. Huber, Z. Liu, S. Bohaty, J. Henderiks, W. Sijp, S. Krishnan, and R. DeConto (2011). The role of carbon dioxide during the onset of Antarctic glaciation. *Science 334*(6060), 1261–1264.

Park, Y., L. Gambéroni, and E. Charriaud (1991). Frontal structure, transport and variability of the Antarctic Circumpolar Current in the South Indian Ocean sector, 40degree-80degreeE. *Marine Chemistry* (35), 45–62.

Park, Y., L. Gambéroni, and E. Charriaud (1993). Frontal structure, water masses, and circulation in the Crozet Basin. *Journal of Geophysical Research* (98), 12361–12385.

Park, Y., F. Roquet, I. Durand, and J. Fuda (2008). Large scale circulation over and around the Northern Kerguelen Plateau. *Deep Sea Research Part II Topical Studies in Oceanography 55*, 566–581.

Park, Y.-H., E. Charriaud, P. Craneguy, and A. Kartavtseff (2001). Fronts, transport, and Weddell Gyre at 30E between Africa and Antarctica. *Journal of Geophysical Research* (106), 2857–2879.

Premoli-Silva, I. and D. Jenkins (1993). Decision on the eocene/oligocene boundary stratotype. *Episodes* (16), 379–382.

Reusch, D. (2002). Oligocene-Miocene terrigenous and pelagic sediments, Skiff Bank, Kerguelen Plateau (ODP Leg 183, Site 1139). In F. Frey, M. Coffin, P. Wallace, and P. Quilty (Eds.), *Proc. ODP, Sci. Results*, Volume 183, pp. 1–31.

Rohling, E. and S. Cooke (1999). Stable oxygen and carbon isotope ratios in foraminiferal carbonate shells. In B. Sen Gupta (Ed.), *Modern Foraminifera*, pp. 239–258. Kluwer Academic.

Rothwell, R. (1989). *Minerals and mineraloids in marine sediments. An optical identification guide.* Elsevier Applied Science.

Ryan, W., S. Carbotte, J. Coplan, S. O'Hara, A. R. Melkonian, A., R. Weissel, V. Ferrini, A. Goodwillie, F. Nitsche, J. Bonczkowski, and R. Zemsky (2009). Global multi-resolution topography synthesis. *Geochem. Geophys. Geosyst* (10).

Salamy, K. and J. Zachos (1999). Latest Eocene-early Oligocene climate change and Southern Ocean fertility: inferences from sediment accumulation and stable isotope data. *Palaeogeography, Palaeoclimatology, Palaeoecology 145*, 61–77.

Scher, H. and E. Martin (2006). Timing and climatic consequences of the opening of Drake Passage. *Science* (312), 428–430.

Schlich, R., J. Wise, S.W., and S. S. Party (1989). *Central Kerguelen Plateau*, Volume 120. College Station, TX (ODP).

Sen Gupta, B. K. (1999). *Modern Foraminifera.*, Chapter 2: Systematics of Modern Foraminifera, pp. 7–35. Kluwer Academic Publishers.

Shackleton, N. (1977). Carbon-13 in Uvigerina: tropical rainforest history and the equatorial Pacific carbonate dissolution cycles. In N. Anderson and A. Malahof (Eds.), *Fate of Fossil Fuel CO_2 in the Oceans.* (Plenum, New York ed.)., pp. 401–427.

Shackleton, N. and N. Opdyke (1973). Oxygen isotope and paleomagnetic stratigraphy of equatorial Pacific core V28-238: oxygen isotope temperatures and ice volumes on a 10^5 and 10^6 year scale. *Quaternary Research* (3), 39–55.

Sijp, W., M. England, and M. Huber (2011). Effect of the deepening of the Tasman Gateway on the global ocean. *Paleoceanography* (26), 1–18.

Sijp, W. P., M. H. England, and J. R. Toggweiler (2009). Effect of ocean gateway changes under greenhouse warmth. *Journal of Climate* (22), 6639–6652.

Stichler, W. (1995). Interlaboratory comparison of new materials for carbon and oxygen ratio measurements. In *Proceedings of a consultants meeting held in Vienna. Organization IAEA-TECDOC-825*, pp. 67–74.

Stickley, C., H. Brinkhuis, S. Schellenberg, A. Sluijs, U. Rhl, M. Fuller, M. Grauert, M. Huber, J. Warnaar, and G. Williams (2004). Timing and nature of the deepening of the tasmanian gateway. *Paleoceanography 19*(4), 1–18.

Stott, L. D. and J. Kennett (1990). Antarctic Paleogene planktonic foraminifer biostratigraphy: ODP Leg 113, Sites 689 and 690. In P. Barker, J. Kennett, and et al. (Eds.), *Proc. ODP, Sci. Results* (College Station, TX (ODP) ed.), Volume 113, pp. 549–569.

Urey, H. (1947). The thermodynamics of isotopic substances. *J. Chem. Soc.*, 562–581.

Urey, H., H. Lowenstam, S. Epstein, and C. McKinney (1951). Measurements of palaeotemperatures and temperatures of the upper Cretaceous of England, Denmark and southeastern United States. *Geological Society of America Bulletin* (62), 399–416.

Van Mourik, C. and H. Brinkhuis (2005). The Massignano Eocene-Oligocene golden spike section revisited. *Stratigraphy 2*(1), 13–30.

Wallace, P., F. Frey, D. Weis, and M. Coffin (2002). Origin and evolution of the Kerguelen Plateau, Broken Ridge and Kerguelen Archipelago: Editorial. *J. Petrol. 43*(7), 1105–1108.

Wei, W. (1992). Paleogene chronology of Southern Ocean drill holes: an update. In J. Kennett and D. Warnke (Eds.), *The Antarctic Paleoenvironment: a Perspective on Global Change.*, Number 56 in Antarct. Res. Ser., pp. 75–96.

Wei, W. and H. Thierstein (1991). Upper Cretaceous and Cenozoic calcareous nannofossils of the Kerguelen Plateau (southern Indian Ocean) and Prydz Bay (East Antarctica). In J. Barron, B. Larsen, and et al. (Eds.), *Proc. ODP, Sci. Results*, Volume 119 of , pp. 467–494. College Station, TX (ODP).

Wei, W. and S. Wise (1990). Selected Neogene calcareous nannofossil index taxa of the Southern Ocean: biochronology, biometrics, and paleoceanography. In S. Wise, R. Schlich, and et al. (Eds.), *Proceedings ODP, Scientific Results*, Volume 120, pp. 523–537. College Station, TX (ODP).

Whitworth, I. T. (1988). The Antarctic Circumpolar Current. *Oceanus* (31), 53–58.

Wise, S. (1983). Mesozoic and Cenozoic calcareous nannofossils recovered by Deep Sea Drilling Project Leg 71 in the Falkland Plateau region, Southwest Atlantic Ocean. In W. Ludwig, V. Krasheninnikov, and et al. (Eds.), *Proc. DSDP, Initial Reports*, Volume 71 (Pt.2), pp. 481–550. Washington (U.S. Govt. Printing Office).

Yang, S., E. Galbraith, and J. Palter (2013). Coupled climate impacts of the Drake Passage and the Panama Seaway. *Climate Dynamics*, 1–16. Springer-Verlag.

Zachos, J., B. Opdyke, T. Quinn, C. Jones, and A. Halliday (1999). Early Cenozoic glaciation, Antarctic weathering, and seawater $^{87}Sr/^{86}Sr$: is there a link? *Chemical Geology* (161), 165–180.

Zachos, J., T. Quinn, and K. Salamy (1996). High-resolution 10^4 years deep-sea foraminiferal stable isotope records of the Eocene-Oligocene climate transition. *Paleoceanography 11*(3), 251–266.

Zachos, J., D. Rea, K. Seto, R. Nomura, and N. Niitsuma (1992). *Synthesis of results from Scientific Drilling in the Indian Ocean*, Chapter Paleogene and early Neogene deepwater paleoceanography of the Indian Ocean as determined from benthic foraminifera stable isotope records, pp. 351–385. Geophysical Monograph. American Geophysical Union.

Zachos, J., L. Stott, and K. Lohmann (1994). Evolution of early Cenozoic marine temperatures. *Paleoceanography 9*(2), 353–387.

Zhang, Z., K. Nisancioglu, F. Flaty, M. Bentsen, I. Bethke, and H. Wang (2011). Tropical seaways played a more important role than high latitude seaways in Cenozoic cooling. *Climate of the Past* (7), 801–813.

Appendices

Appendix A

Visual core description

A.1 Site 1138

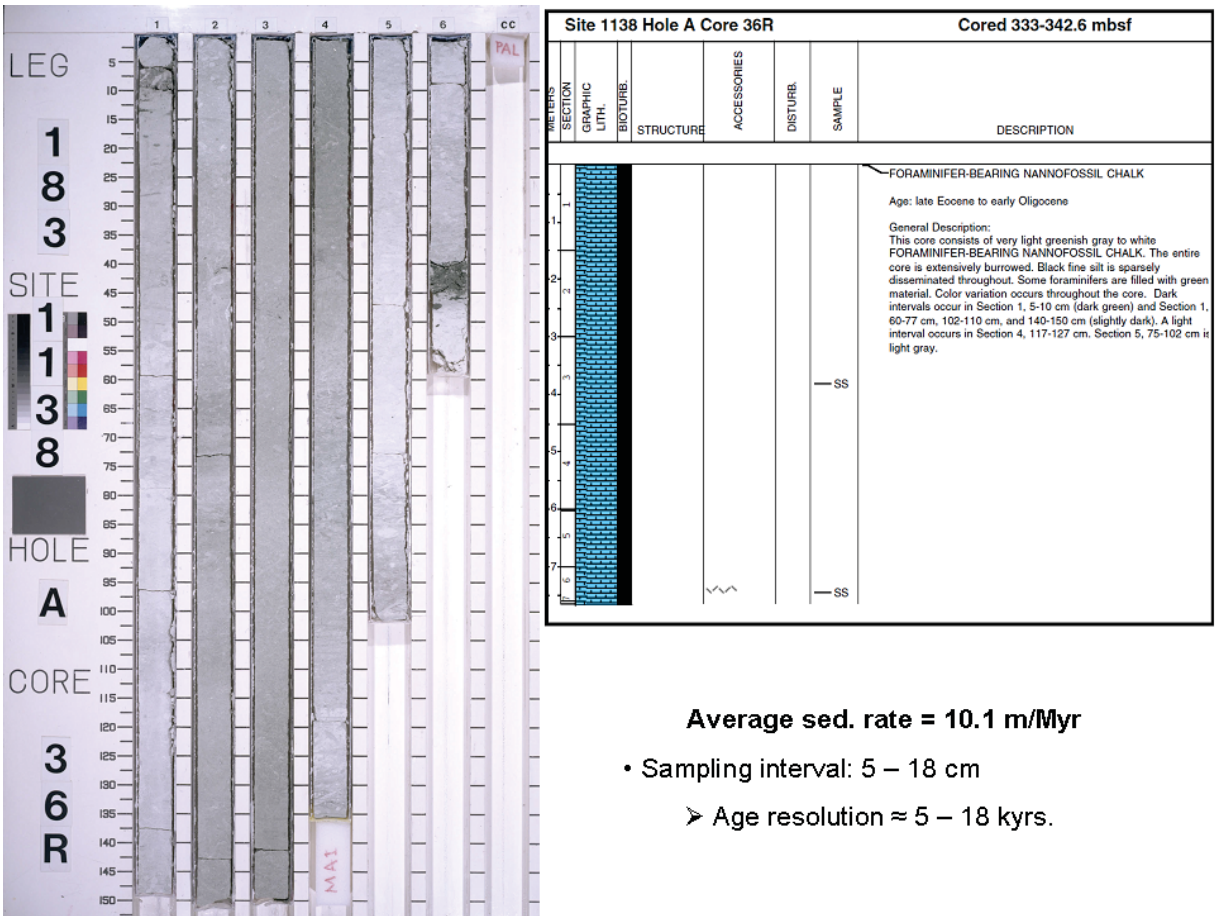

Figure A.1: Site 1138 visual and lithological core description from which the samples have been retrieved. Taken from Coffin et al. (2000). Also shown are sampling intervals and calculated resolution based from the chosen sedimentation rate from the age model.

A.2 Site 1139

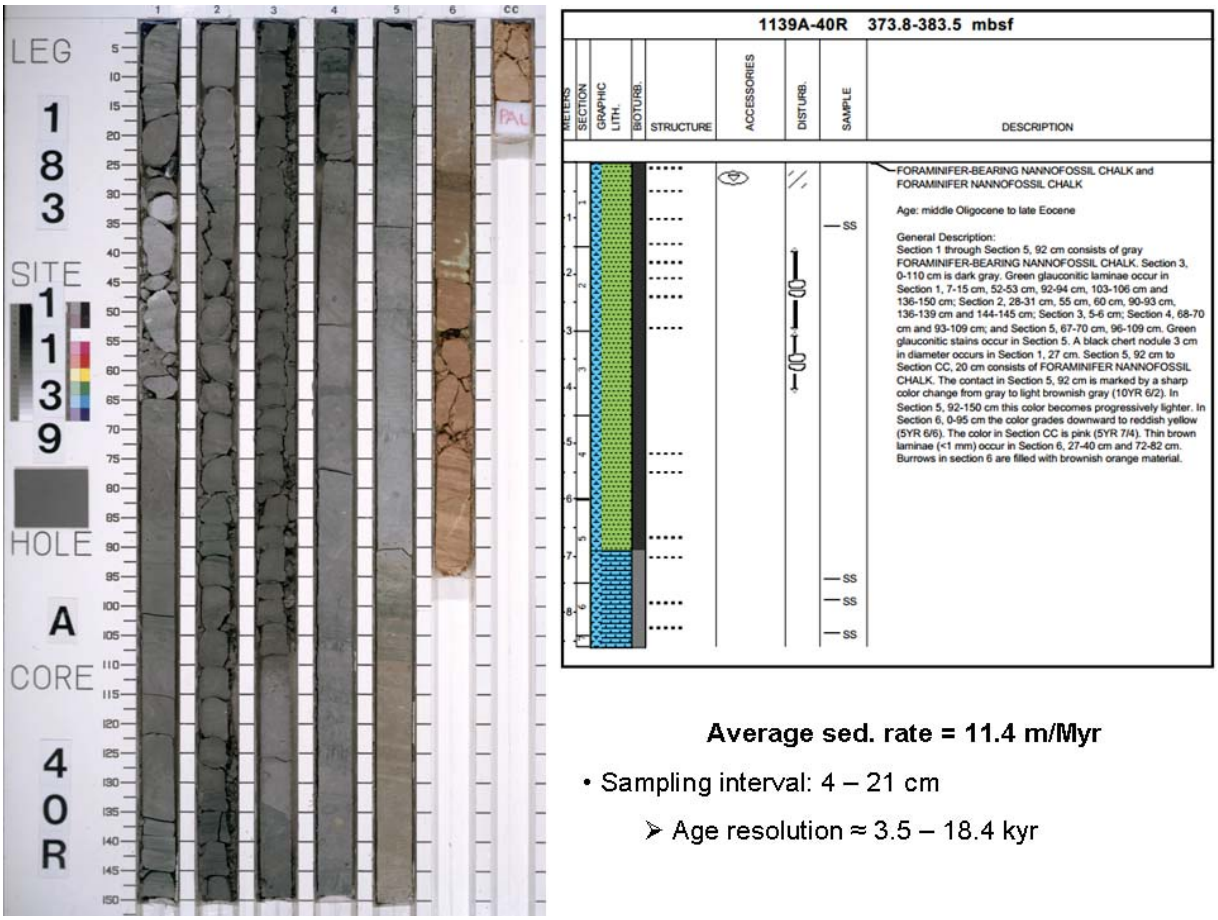

Figure A.2: Site 1139 visual and lithological core description from which the samples have been retrieved. Taken from Coffin et al. (2000). Also shown are sampling intervals and calculated resolution based from the chosen sedimentation rate from the age model.

A.3 Site 1140

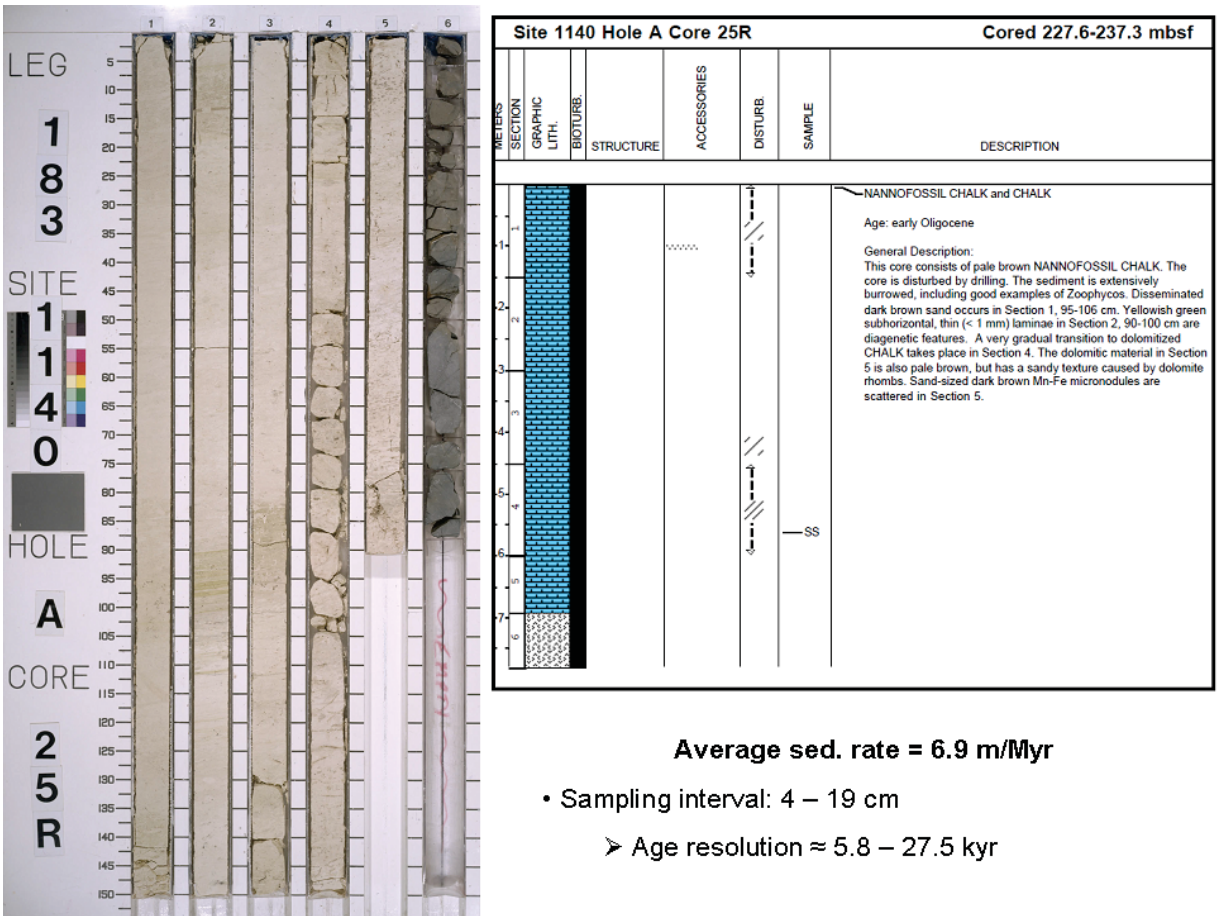

Figure A.3: Site 1140 visual and lithological core description from which the samples have been retrieved. Taken from Coffin et al. (2000). Also shown are sampling intervals and calculated resolution based from the chosen sedimentation rate from the age model.

Appendix B

Stable isotope data

Site 1138 - *Cibicidoides mundulus*							
sample no.	**Top Core Depth sample source [cm]**	**specimens picked**	**mass [g]**	**size range [m]**	**d13C**	**d18O**	**Depth [mbsf]**
1	1138A-36R-2, 75-77	15	0.187	150 - 250	0.87	1.31	335.25
2	1138A-36R-2, 88-90	16	0.188	150 - 250	0.85	1.20	335.38
3	1138A-36R-2, 103-105	15	0.192	150 - 250	0.88	1.02	335.53
4	1138A-36R-2, 112.5-114.5	16	0.187	150 - 250	0.92	1.15	335.625
5	1138A-36R-2, 123.5-125.5	15	0.192	150 - 250	1.13	1.29	335.735
6	1138A-36R-2, 136-138	15	0.186	150 - 250	1.02	1.24	335.86
7	1138A-36R-2, 148-150	13	0.191	150 - 250	0.91	1.29	335.98
8	1138A-36R-3, 3-5	17	0.200	150 - 250	0.79	1.39	336.03
9	1138A-36R-3, 15-17	15	0.188	150 - 250	0.90	1.41	336.15
10	1138A-36R-3, 27.5-29.5	16	0.199	150 - 250	0.95	1.24	336.275
11	1138A-36R-3, 36.5-38.5	16	0.202	150 - 250	1.01	1.51	336.365
12	1138A-36R-3, 48-50	15	0.199	150 - 250	1.05	1.44	336.48
13	1138A-36R-3, 62-64	18	0.192	150 - 250	0.85	1.44	336.62
14	1138A-36R-3, 75-77	17	0.206	150 - 250	0.92	1.53	336.75
15	1138A-36R-3, 88-90	15	0.187	150 - 250	1.11	1.49	336.88
16	1138A-36R-3, 102-104	17	0.188	150 - 250	0.95	1.74	337.02
17	1138A-36R-3, 112-114	17	0.201	150 - 250	1.05	1.36	337.12
18	1138A-36R-3, 126-128	15	0.189	150 - 250	0.88	1.36	337.26
19	1138A-36R-3, 136-138	18	0.196	150 - 250	1.00	0.97	337.36
20	1138A-36R-3, 147-149	19	0.202	150 - 250	0.97	1.49	337.47
21	1138A-36R-4, 3-5	16	0.197	150 - 250	1.02	1.89	337.53
22	1138A-36R-4, 15-17	17	0.191	150 - 250	1.07	1.52	337.65
23	1138A-36R-4, 27.5-29.5	16	0.196	150 - 250	1.12	1.59	337.775
24	1138A-36R-4, 39-41	16	0.183	150 - 250	1.06	1.65	337.89
25	1138A-36R-4, 52-54	14	0.195	150 - 250	1.14	1.68	338.02
26	1138A-36R-4, 61.5-63.5	16	0.190	150 - 250	1.20	1.70	338.115
27	1138A-36R-4, 75-77	16	0.206	150 - 250	1.25	1.87	338.25
28	1138A-36R-4, 88-90	16	0.187	150 - 250	1.36	1.88	338.38
29	1138A-36R-4, 102-104	15	0.194	150 - 250	1.46	1.90	338.52
30	1138A-36R-4, 112-114	17	0.206	150 - 250	1.07	1.59	338.62
31	1138A-36R-4, 125-127	17	0.195	150 - 250	0.99	1.37	338.75
32	1138A-36R-4, 134-136	17	0.193	150 - 250	1.04	1.30	338.84
33	1138A-36R-5, 3-5	18	0.198	150 - 250	1.06	1.42	339.03
34	1138A-36R-5, 15-17	16	0.186	150 - 250	1.00	1.19	339.15
35	1138A-36R-5, 27-29	16	0.190	150 - 250	0.94	1.20	339.27
36	1138A-36R-5, 38.5-40.5	16	0.200	150 - 250	1.01	1.41	339.385
37	1138A-36R-5, 54-56	17	0.207	150 - 250	0.99	1.48	339.54
38	1138A-36R-5, 63-65	15	0.182	150 - 250	1.00	1.24	339.63
39	1138A-36R-5, 75-77	18	0.181	150 - 250	0.81	1.15	339.75
40	1138A-36R-5, 88-90	17	0.195	150 - 250	0.92	1.34	339.88
41	1138A-36R-5, 98-100	16	0.199	150 - 250	0.95	1.37	339.98
42	1138A-36R-6, 2.5-4.5	18	0.199	150 - 250	0.81	1.43	340.025
43	1138A-36R-6, 14-16	17	0.195	150 - 250	0.85	1.34	340.14
44	1138A-36R-6, 26-28	18	0.183	150 - 250	0.55	1.19	340.26
45	1138A-36R-6, 35-37	18	0.200	150 - 250	0.49	1.29	340.35
46	1138A-36R-6, 53-55	19	0.185	150 - 250	0.85	0.92	340.53
47	1138A-36R-CC	16	0.204	150 - 250	0.86	1.25	340.6

Site 1139 - *Cibicidoides mundulus*								
sample no.	**Top Core Depth sample source [cm]**	**specimens picked**	**mass [g]**	**size range [m]**	**d13C**	**d18O**	**Depth [mbsf]**	Comments
48	1139A-40R-1, 63 - 65	16	0.202	150-250	0.63	0.94	374.43	
49	1139A-40R-1, 78 - 80	18	0.205	150-250	0.70	1.00	374.58	
50	1139A-40R-1, 89 - 91	16	0.204	150-250	0.60	1.02	374.69	
51	1139A-40R-1, 101 - 103	14	0.19	150-250	0.80	0.64	374.81	
52	1139A-40R-1, 114 - 116	11	0.2	150-250	0.95	0.81	374.94	
53	1139A-40R-1, 126 - 128	12	0.205	150-250	0.99	0.94	375.06	
54	1139A-40R-1, 147 - 149	17	0.204	150-250	0.91	0.63	375.27	
55	1139A-40R-2, 3 - 5	13	0.194	150-250	0.87	0.98	375.33	
56	1139A-40R-2, 15 - 17	17	0.198	150-250	0.92	0.82	375.45	
57	1139A-40R-2, 31 - 33	14	0.183	150-250	0.94	0.70	375.61	
58	1139A-40R-2, 39 - 41	15	0.183	150-250	0.85	0.65	375.69	
59	1139A-40R-2, 49 - 51	15	0.205	150-250	0.85	0.79	375.79	
60	1139A-40R-2, 63 - 65	14	0.193	150-250	0.73	0.57	375.93	
61	1139A-40R-2, 73 - 75	14	0.202	150-250	0.63	-0.09	376.03	
62	1139A-40R-2, 87 - 89	18	0.185	150-250	0.79	0.13	376.17	
63	1139A-40R-2, 98 - 100	17	0.183	150-250	0.93	0.80	376.28	
64	1139A-40R-2, 111 - 113	14	0.188	150-355	1.05	0.87	376.41	
65	1139A-40R-2, 123 - 125	18	0.205	150-250	0.77	0.79	376.53	
66	1139A-40R-2, 135 - 137	16	0.213	150-250	0.83	0.60	376.65	
67	1139A-40R-2, 147 - 149	15	0.201	150-355	0.77	0.72	376.77	
68	1139A-40R-3, 6 - 8	15	0.12	150-250	0.77	0.68	376.86	small vial
69	1139A-40R-3, 15 - 17	12	0.197	150-355	0.72	0.98	376.95	
70	1139A-40R-3, 27 - 29	12	0.203	150-355	0.68	0.86	377.07	
71	1139A-40R-3, 40 - 42	9	0.125	150-355	0.83	0.93	377.2	small vial
72	1139A-40R-3, 49 - 51	10	0.119	150-250	0.74	0.46	377.29	small vial
73	1139A-40R-3, 60 - 62	12	0.134	150-355	0.83	0.87	377.4	small vial
74	1139A-40R-3, 72 - 74	18	0.109	63-250	0.83	0.17	377.52	small vial
75	1139A-40R-3, 88 - 90	9	0.113	150-250	0.83	0.20	377.68	small vial
76	1139A-40R-3, 96 - 98	7	0.096	150-250	0.74	0.41	377.76	small vial
77	1139A-40R-3, 109 - 111	6	0.098	150-355	0.87	0.53	377.89	small vial
78	1139A-40R-3, 121 - 123	9	0.087	150-250	0.61	0.55	378.01	small vial
79	1139A-40R-3, 132 - 134	6	0.132	150-355	0.64	0.97	378.12	small vial
80	1139A-40R-3, 144 - 146	6	0.082	150-355	0.71	0.69	378.24	small vial
81	1139A-40R-4, 2 - 4	5	0.224	150-425	0.25	0.81	378.32	
82	1139A-40R-4, 15 - 17	5	0.186	150-355	0.38	0.80	378.45	
83	1139A-40R-4, 29 - 31	6	0.2	63-355	0.51	0.85	378.59	
84	1139A-40R-4, 39 - 41	10	0.187	150-250	0.59	0.73	378.69	
85	1139A-40R-4, 50 - 52	11	0.212	150-355	0.45	0.39	378.8	
86	1139A-40R-4, 63 - 65	7	0.101	150-355	0.59	0.25	378.93	small vial
87	1139A-40R-4, 75 - 77	3	0.114	150-355	0.61	0.46	379.05	small vial
88	1139A-40R-4, 87 - 89	4	0.212	150-355	0.29	0.09	379.17	
89	1139A-40R-4, 98.5 - 100.5	4	0.239	150-355	0.21	0.52	379.285	
90	1139A-40R-4, 111 - 113	4	0.208	150-355	0.29	0.00	379.41	
91	1139A-40R-4, 123 - 125	4	0.128	150-250	0.28	0.41	379.53	small vial
92	1139A-40R-4, 135 - 137	7	0.21	250-355	0.24	0.48	379.65	
93	1139A-40R-4, 147 - 149	5	0.226	250-355	0.16	0.45	379.77	
94	1139A-40R-5, 3 - 5	7	0.128	150-355	0.45	0.81	379.83	small vial
95	1139A-40R-5, 15 - 17	5	0.098	63-355	0.69	0.66	379.95	small vial
96	1139A-40R-5, 28 - 30	6	0.103	150-355	0.35	0.35	380.08	small vial
97	1139A-40R-5, 39 - 41	14	0.203	150-250	0.47	0.94	380.19	
98	1139A-40R-5, 53 - 55	13	0.232	150-250	0.54	1.11	380.33	
99	1139A-40R-5, 63 - 65	12	0.196	150-250	0.56	0.95	380.43	
100	1139A-40R-5, 79 - 81	14	0.214	150-250	0.42	1.16	380.59	
101	1139A-40R-5, 88 - 90	11	0.194	150-355	0.46	1.13	380.68	
102	1139A-40R-5, 101 - 103	4	0.222	355-425	0.59	1.14	380.81	
103	1139A-40R-5, 111 - 113	6	0.106	150-355	0.79	0.94	380.91	small vial
104	1139A-40R-5, 123 - 125	9	0.136	150-355	0.67	1.18	381.03	small vial
105	1139A-40R-5, 135 - 137	9	0.095	150-250	0.75	1.00	381.15	small vial
106	1139A-40R-5, 147 - 149	21	0.201	150-250	0.71	1.03	381.27	
107	1139A-40R-6, 3 - 5	20	0.191	150-250	0.72	1.13	381.33	
108	1139A-40R-6, 13 - 15	17	0.196	150-250	0.76	0.55	381.43	
109	1139A-40R-6, 20 - 22	9	0.091	150-250	0.95	0.72	381.5	small vial
110	1139A-40R-6, 31 - 33	8	0.09	150-250	0.79	0.85	381.61	small vial
111	1139A-40R-6, 39.5 - 41.5	16	0.191	150-250	0.88	1.14	381.695	
112	1139A-40R-6, 51 - 53	21	0.217	150-250	0.90	1.28	381.81	
113	1139A-40R-6, 63 - 65	18	0.212	150-250	1.07	1.31	381.93	
114	1139A-40R-6, 75 - 79	11	0.101	150-250	1.12	1.36	382.05	small vial
115	1139A-40R-6, 90 - 92	20	0.188	150-250	1.30	1.21	382.2	
116	1139A-40R-CC, 10 - 12	18	0.222	150-250	0.89	0.43	382.32	

Site 1139 - *Cibicidoides mundulus*								
sample no.	**Top Core Depth sample source [cm]**	**specimens picked**	**mass [g]**	**size range [m]**	**d13C**	**d18O**	**Depth [mbsf]**	Comments
117	1140A-24R-5, 42 - 44	13	0.212	250-150	0.85	0.94	223.92	
118	1140A-24R-5, 50 - 52	13	0.208	250-150	0.83	0.19	224	
119	1140A-24R-5, 69 - 71	15	0.197	250-150	1.09	0.78	224.19	
120	1140A-24R-CC, 2 - 4	15	0.204	250-150	1.04	0.96	224.26	
121	1140A-24R-CC, 13 - 15	15	0.214	250-150	1.08	1.07	224.37	
122	1140A-25R-1, 5 - 7	18	0.194	250-150	1.07	0.94	227.65	
123	1140A-25R-1, 18 - 20	18	0.224	250-150	1.11	1.22	227.78	
124	1140A-25R-1, 28 - 30	17	0.221	250-150	0.97	0.93	227.88	
125	1140A-25R-1, 41 - 43	17	0.2O7	250-150	1.36	1.18	228.01	
126	1140A-25R-1, 54 - 56	16	0.197	250-150	1.31	1.10	228.14	
127	1140A-25R-1, 65 - 67	15	0.2	250-150	1.22	1.13	228.25	
128	1140A-25R-1, 79 - 81	17	0.193	250-150	1.35	1.26	228.39	
129	1140A-25R-1, 98 - 100	19	0.213	250-150	1.31	1.20	228.58	
130	1140A-25R-1, 112 - 114	17	0.195	250-150	1.41	1.21	228.72	
131	1140A-25R-1, 123 - 125	16	0.222	250-150	1.36	1.44	228.83	
132	1140A-25R-1, 135 - 137	15	0.201	250-150	1.44	1.30	228.95	
133	1140A-25R-1, 147 - 149	16	0.23	250-150	1.40	1.49	229.07	
134	1140A-25R-2, 4 - 6	15	0.19	250-150	1.34	1.29	229.14	
135	1140A-25R-2, 16 - 18	15	0.222	250-150	1.37	1.48	229.26	
136	1140A-25R-2, 27 - 29	13	0.196	250-150	1.40	1.39	229.37	
137	1140A-25R-2, 40 - 42	18	0.197	250-150	1.31	1.26	229.5	
138	1140A-25R-2, 54 - 56	17	0.207	250-150	1.35	1.66	229.64	
139	1140A-25R-2, 64 - 66	16	0.209	250-150	1.37	1.60	229.74	
140	1140A-25R-2, 79 -81	17	0.188	250-150	1.33	1.50	229.89	
141	1140A-25R-2, 88 - 90	18	0.192	250-150	1.23	1.50	229.98	
142	1140A-25R-2, 98 - 100	18	0.208	250-150	1.36	1.65	230.08	
143	1140A-25R-2, 112 - 114	18	0.199	250-150	1.34	1.68	230.22	
144	1140A-25R-2, 123 - 125	18	0.189	250-150	1.41	1.47	230.33	
145	1140A-25R-2, 136 - 138	17	0.217	250-150	1.48	1.72	230.46	
146	1140A-25R-2, 148 - 150	17	0.186	250-150	1.37	1.56	230.58	
147	1140A-25R-3, 12 - 14	17	0.195	250-150	1.44	1.55	230.72	
148	1140A-25R-3, 22 - 24	19	0.197	250-150	1.54	1.50	230.82	
149	1140A-25R-3, 34 - 36	18	0.197	250-150	1.56	1.33	230.94	
150	1140A-25R-3, 46 - 48	18	0.217	250-150	1.60	1.76	231.06	
151	1140A-25R-3, 58 - 60	18	0.219	250-150	1.63	1.69	231.18	
152	1140A-25R-3, 70 - 72	17	0.188	250-150	1.56	1.66	231.3	
153	1140A-25R-3, 82 - 84	17	0.226	250-150	1.60	1.74	231.42	
154	1140A-25R-3, 94 - 96	15	0.192	250-150	1.56	1.61	231.54	
155	1140A-25R-3, 106 - 108	16	0.195	250-150	1.66	1.82	231.66	
156	1140A-25R-3, 118 - 120	18	0.202	250-150	1.68	1.39	231.78	
157	1140A-25R-3, 129.5 - 131.5	17	0.229	250-150	1.64	1.22	231.895	
158	1140A-25R-3, 142 - 144	19	0.212	250-150	1.50	1.39	232.02	
159	1140A-25R-4, 7 - 9	20	0.215	250-150	1.20	0.93	232.17	
160	1140A-25R-4, 16 - 18	20	0.209	250-150	1.21	1.07	232.26	
161	1140A-25R-4, 30 - 32	18	0.204	250-150	1.20	0.83	232.4	
162	1140A-25R-4, 38 - 40	18	0.194	250-150	1.24	0.82	232.48	
163	1140A-25R-4, 54 - 56	18	0.195	250-150	1.09	0.76	232.64	
164	1140A-25R-4, 65 - 67	22	0.203	250-150	1.12	0.69	232.75	
165	1140A-25R-4, 75 - 77	19	0.204	250-150	1.05	0.76	232.85	
166	1140A-25R-4, 84 - 86	19	0.209	250-150	1.16	0.91	232.94	
167	1140A-25R-4, 100 - 102	16	0.213	250-150	1.26	0.96	233.1	
168	1140A-25R-4, 114 - 116	15	0.186	250-150	1.08	0.68	233.24	
169	1140A-25R-4, 123.5 - 125.5	16	0.187	250-150	1.04	0.71	233.335	
170	1140A-25R-4, 133.5 - 135.5	16	0.198	250-150	0.89	0.76	233.435	
171	1140A-25R-4, 146 - 148	18	0.199	250-150	1.04	0.77	233.56	
172	1140A-25R-5, 10 - 12	8	0.08	250-150	0.97	0.89	233.7	small vial
173	1140A-25R-5, 22 - 24	17	0.206	250-150	1.09	0.88	233.82	
174	1140A-25R-5, 34 - 36	17	0.19	250-150	1.14	0.66	233.94	
175	1140A-25R-5, 44.5 - 46.5	16	0.214	250-150	1.13	0.83	234.045	
176	1140A-25R-5, 58 - 60	12	0.108	250-150	1.03	1.29	234.18	small vial
177	1140A-25R-5, 71 - 73	10	0.119	250-150	1.02	1.34	234.31	small vial
178	1140A-25R-5, 82 - 84	12	0.215	250-150	1.06	1.35	234.42	
179	1140A-25R-5, 86 -90	5	0.133	250-150	1.15	1.90	234.46	small vial
180	1140A-25R-CC	4	0.1	250-150	0.84	1.10	234.5	small vial